Chapter 5

Chapter 5

Surface plasmon resonance enhanced Z-scheme photocatalysis using Ag integrated heterojunction of an emerging semiconductor

The previous chapter reports on a plasmonic-heterojunction photocatalytic system with significantly enhanced dye degradation under visible light, due to suppressed charge recombination, extended light absorption, and plasmonic near-field enhancement. To further investigate the role of surface plasmon resonance in enhancing photocatalytic performance, this chapter presents a novel photocatalyst system featuring Ag nanoparticles integrated into a heterojunction of underexplored host semiconductors. Thus, a plasmonic-based photocatalyst, Ag@NiO/Ag_2CrO_4, was developed through the integration of Ag metal during the synthesis of Ni-Cr LDH. The catalyst synthesis involved the modification of Ni-Cr LDH through the addition of a metallic Ag solution, followed by air heat treatment, leading to the in-situ formation of the mixed metal oxide Ag@NiO/Ag_2CrO_4 along wiith traces of spinel $NiCr_2O_4$ that was detected only in Raman analysis and in XPS where +3 oxidation state of Cr matches to that of Cr in $NiCr_2O_4$. The photocatalyst exhibits strong visible-light absorption and suitably positioned band edges, forming a Z-scheme heterojunction that facilitates efficient charge transfer and enhances redox reactivity. This mechanism has been systematically confirmed through UV-DRS, VB-XPS, TRPL, and Mott-Schottky analysis. The photocatalytic performance was assessed by the degradation of MB and RhB dye, revealing that the heterojunction photocatalyst outperformed the pristine counterparts. The enhanced catalytic performance can be attributed to three key factors: the layered morphology of the photocatalyst, efficient visible-light absorption, and the plasmonic effects of Ag nanoparticles. This chapter also reveals a significant finding: Ag nanoparticles facilitate plasmon-induced resonance energy transfer (PIRET), which plays a pivotal role in sustaining efficient Z-scheme charge transfer between Ag_2CrO_4 and NiO. This mechanism enhances visible-light-driven activity by effectively activating NiO.

5.1. Introduction

In the quest for effective photocatalytic materials, silver-based compounds, particularly Ag_2WO_4, Ag_2MoO_4, and Ag_2CrO_4 have garnered considerable interest owing to their distinctive photosensitivity, which imparts exceptional light absorption capabilities and

facilitate visible light activated catalytic processes [1-4]. Ag_2CrO_4 distinguishes itself among silver-based semiconductors due to its wide spectral absorption range, and efficient photogenerated carrier transfer, which offer a significant advantage in photocatalytic applications. The distinct crystalline structure and electronic configuration of Ag_2CrO_4 promote the participation of photogenerated charge carriers, resulting in efficient generation of reactive oxygen species (ROS) [2, 5]. Nonetheless, the limited efficiency of unmodified Ag_2CrO_4 catalysts, due to poor photogenerated carrier separation, restricts their vast application [6, 7]. Studies have shown that strategies such as element substitution, morphology tuning, and heterojunction formation can significantly alleviate this issue [5, 7-9]. A study shows that Eu^{3+} doping enhances the photocatalytic efficiency and stability of Ag_2CrO_4 by modifying its band structure, which improves charge separation and supports multiple degradation pathways, significantly boosting its photocatalytic ability under visible light [4]. In a recent study, Gorouhi et al. investigated double Z-scheme Ag_2CrO_4/Bi_2O_3-KBi_6O_9Br catalysts for the degradation of various organic dyes [10]. Their findings revealed that the double Z-scheme interface between the catalysts significantly enhanced charge separation, thereby boosting overall photocatalytic performance. In a separate study, the $Ag/Ag_2CrO_4/g$-C_3N_4 catalyst was used to degrade wastewater laden with tetracycline and quinolone compounds [9]. The findings indicated that the mesoporous g-C_3N_4 framework effectively supported Ag and Ag_2CrO_4 nanoparticles, providing additional active sites, while the plasmon resonance effect combined with a synergistic Z-scheme heterojunction strategy offered significant advantages within the composite, thereby enhancing the degradation of organic pollutants.

Among various enhancement strategies, two-dimensional (2D) nanostructures, commonly used as co-catalysts with semiconductor photocatalysts, significantly boost photocatalytic efficiency [11-13]. Purposeful optimization of tailored photocatalyst structures and surface properties has proven to be a powerful approach for advancing oxidation reactions in photocatalysis. Layered double hydroxides (LDHs) are emerging as an attractive group of 2D structures for solar energy conversion, driven by their distinctive physicochemical properties, including a modifiable layered architecture, compositional adaptability, tunable bandgaps, advantages from oxygen vacancies, facile synthetic routes, and low production costs [14-17]. LDHs constitute a family of anionic

clay minerals featuring alternating layers of mixed-valent metal hydroxides and charge-compensating interlayer anions. These materials, isostructural with naturally occurring hydrotalcite, contain both divalent (M^{2+}) and trivalent (M^{3+}) cations in their brucite-like layers, with interstitial anions maintaining charge neutrality [18-20]. Because of its 2D layered structure, LDH materials have charge transport properties highly suitable for photo- and electro-catalysis [20]. The lamellar structure of LDH is known to collapse upon calcination, yielding thermally stable mixed oxide phases [18]. However, when the collapsed LDH comes into contact with abundant surrounding moisture in the environment, the former lamellar structure is regained. This memory effect of the LDH is advantageous, as it may facilitate the adsorption of dye or water molecules within the interlamellar spaces, thereby providing additional active sites for oxidation and reduction reactions to occur. Other attractive properties of LDHs include facile anion exchange, exceptional anion uptake capacity, straightforward synthesis process, and economic production feasibility [19]. However, the use of LDHs as photocatalysts is still not very common because of their low efficiency, even though their light absorption range is broader compared to photocatalysts such as TiO_2.

This chapter demonstrates a novel plasmonic-based photocatalyst developed through the integration of Ag metal onto Ni-Cr LDH, highlighting its photocatalytic efficiency and comprehensive characterization. The synthesis steps of Ni-Cr LDH were followed until, at a specific stage, Ag metallic solution was incorporated, forming a slurry that, upon calcination, yielded a mixed metal oxide system $Ag@NiO/Ag_2CrO_4$. The $Ag@NiO/Ag_2CrO_4$ photocatalyst exhibits a strong visible light absorption, particularly with the plasmonic resonance peak of Ag. The band edge alignments relevant to redox reactions and the nature of the heterojunction were systematically investigated. Photocatalytic performance was evaluated through the degradation of methylene blue (MB) and rhodamine B (RhB), revealing enhanced activity attributable to several contributing factors, which are discussed in detail in this chapter.

5.2. Experimental details

5.2.1. Materials and methods

Nickel nitrate hexahydrate [$Ni(NO_3)_2.6H_2O$] was supplied by Merck, India. Chromium Nitrate Nonahydrate [$Cr(NO_3)_3.9H_2O$, 97% purity] and Sodium Chromate Tetrahydrate [$Na_2CrO_4.4H_2O$, 99%] were received from Loba Chemie Pvt. Ltd. Sodium

Hydroxide (NaOH) was purchased from Avantor Performance Materials India Ltd. Polyvinyl Pyrolidone (PVP) from Himedia Laboratories Pvt. Ltd, India. Sodium Carbonate Anhydrous (Na_2CO_3), Tri-sodium Citrate Dihydrate (TSC, $C_6H_5Na_3O_7.2H_2O$), and Sodium Borohydrate ($NaBH_4$) were obtained from Merck Life Science Private Limited. Silver Nitrate ($AgNO_3$), and Hydrogen Peroxide (H_2O_2) were provided by Thermo Fisher Scientific India Pvt. Ltd.

The Ag nanoparticle colloidal suspension was prepared in the following steps. Initially, 0.0703 g of $AgNO_3$ was solubilized in 50 mL of doubly distilled (DD) water. 1.5 mL of PVP solution was added to it by stirring, followed by 1.5 mL of TSC. Next, 60 µL H_2O_2 was introduced as an etching agent in the solution using a micropipette. After a while, the silver ions in the mixture were finally reduced to silver metal particles by the introduction of 9 mL $NaBH_4$ solution, which was done by adding 1 mL aliquots after every 2s to the mixture.

Ni-Cr LDH was prepared by using 0.02 M of $Ni(NO_3)_2.6H_2O$ and 0.01 M of $Cr(NO_3)_3.9H_2O$ as precursors in 100 mL of DD water. After ensuring the proper mixing of precursors by continuous stirring, 100 mL of 0.01 M $NaCO_3$ was introduced in 1 mL aliquots to the reaction mixture under vigorous stirring. A few moments after the addition of $NaCO_3$, 100 mL of NaOH (1 M) solution was introduced dropwise to the homogeneous solution. This homogeneous solution was allowed 16 hours of thermal aging at 65 ºC with mechanical stirring, and finally, the pH was carefully adjusted to 7-8. The suspension was filtered, and the collected solids were dried, ground, and calcined at 600 ºC.

Preparation of $Ag@NiO/Ag_2CrO_4$ follows the same procedures as adopted in the synthesis of Ni-Cr LDH up to the addition of $NaCO_3$ solution. Subsequently, a pre-prepared Ag colloidal suspension was introduced to the suspension, and after 15 minutes, NaOH solution was subsequently added. All the subsequent steps, as outlined in the Ni-Cr LDH synthesis, were then followed again. Finally, the precipitate was collected, dried, ground to get the powder form, and then calcined at 600º C. The products obtained after calcination at 600 ºC are designated as NC for Ni-Cr LDH and ANC for $Ag@NiO/Ag_2CrO_4$. A block diagram representation of the synthesis procedure is provided in Figure 5.1.

To prepare the Ag_2CrO_4 catalyst, 0.2323 g of $Na_2CrO_4.4H_2O$ was solubilized in 50 mL of DD water to obtain a yellowish solution. Meanwhile, the $AgNO_3$ solution was separately prepared by mixing 0.0516 g of $AgNO_3$ in 50 mL of DD water. While putting the chromate salt solution under vigorous stirring, the silver nitrate solution was added dropwise onto it, causing the mixture to gradually turn reddish as the drops were introduced. The mixture was continuously stirred for an additional 2 hours, after which the precipitate was collected, thoroughly washed, and dried.

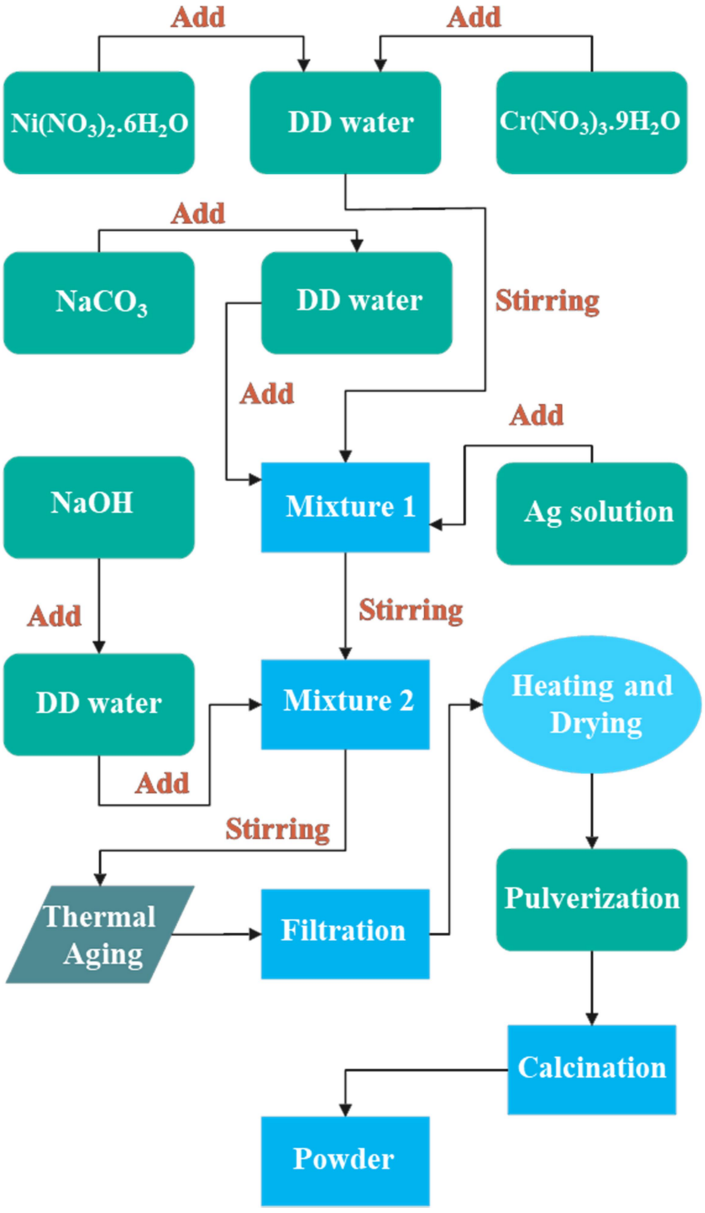

Figure 5.1. Block diagram illustrating the synthesis of Ag@NiO/Ag_2CrO_4.

For the synthesis of the NiO counterpart, initially, four solutions were independently prepared in four separate beakers as follows: 1.163 g of $Ni(NO_3)_2.6H_2O$ was dissolved in 100 mL DD water, 0.064 g of PVP was dissolved in 100 mL DD water, 4 g of NaOH was prepared in 100 mL DD water, and 0.101 g of Na_2CO_3 was thoroughly mixed in 100 mL DD water. While keeping the nitrate solution under stirring, 1.5 mL of PVP solution was added to it, followed by the addition of the entire Na_2CO_3 and NaOH solution in sequence. The solutions were added using a micropipette in 1 mL aliquots, except for NaOH, which was added in droplets. The resultant mixture was kept under stirring for 24 hours, and then the pH was adjusted to 7 before the collection of the precipitate by centrifugation. The dried solid precipitate was then ground and calcined at 600 ºC to get the NiO in powder form.

For the preparation of Ag@NiO, an already prepared Ag solution was added to a dispersed NiO suspension of 50 mL DD water, which was continuously stirred for 24 hours. The precipitate was collected, dried and labeled as AN.

5.2.2. Characterization

The photocatalysts were characterised using the following analysis techniques: XRD, UV-visible DRS, Raman, Photoluminescence, XPS, SEM, TEM, TRPL and Mott-Schottky. The details of the instrument for the technique have been given in Chapter 2. The photocatalytic performance of the photocatalysts was evaluated against MB and RhB dye degradation following the procedures as described in Chapter 2.

5.3. Results and discussion

5.3.1. Structural and optical characterization

XRD results of the mixed-metal oxides NC, AC, and ANC are presented in Figure 5.2. The diffraction pattern of NC (Ni-Cr LDH 600 ºC) shows peaks corresponding to the NiO-like phase (JCPDS card no: 04-0835) at 2θ = 37.1º, 43.6º, and 63.4º with their corresponding crystal planes labeled as (111), (200), and (220), respectively [21-22]. Similar types of broad peaks are also observed in ANC at the same 2θ positions, indicative of the same changes that took place after the calcination of raw Ni-Cr layered double hydroxides to form NC and ANC [21-22]. The crystalline phases of pristine Ni-Cr and Ag@Ni-Cr LDH were identified through XRD, as shown in Figure 5.3. Moreover, there are peaks in ANC whose positions coincide with the peak positions of

AC (as prepared Ag_2CrO_4) at 2θ = 17.3º, 21.5º, 25.1º, 31.1º, 32.1º, 33.4º, 39.1º, 44.1º, 45.1º, 47.8º, 52.0º, 55.8º, 56.8º, 61.7º, and 62.4º. These peaks are identified as representing the XRD pattern of Ag_2CrO_4 (PDF no: 026-0952) [23].

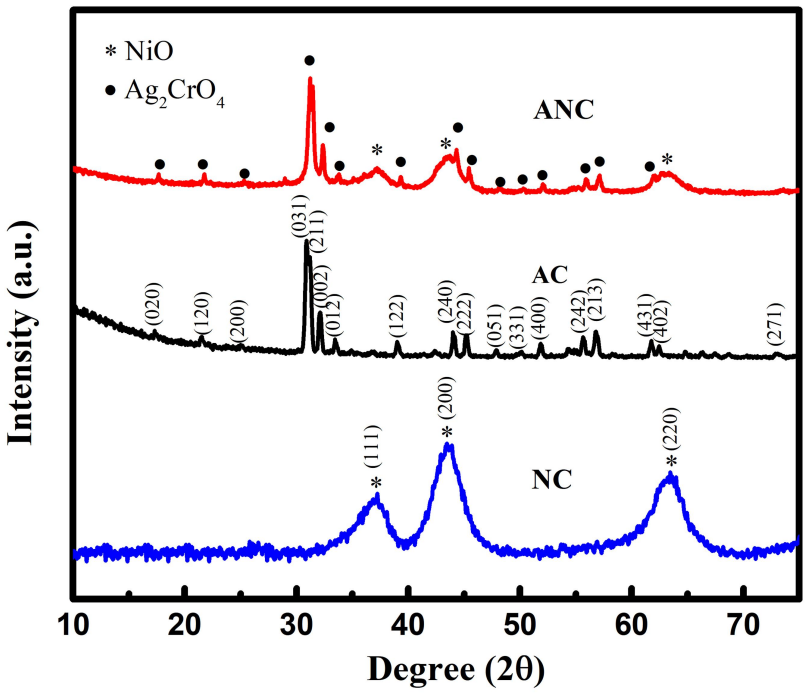

Figure 5.2. X-ray diffraction spectra of NC, AC, and ANC.

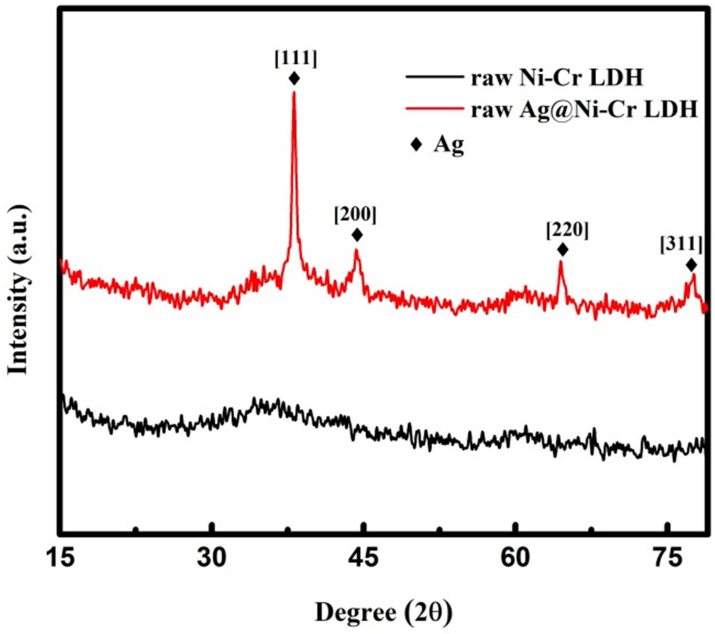

Figure 5.3. X-ray diffraction spectra of raw Ni-Cr LDH and Ag@Ni-Cr LDH.

The corresponding planes are (020), (120), (200), (031), (002), (012), (122), (240). (222), (051), (400), (242), (213), (431), and (402), respectively. The mean crystallite dimensions were calculated to be ~3.6 nm, ~16.1 nm, and ~29 nm for NC, AC, and ANC, respectively, from the equation 2.2.

The UV-vis DRS spectra of the photocatalysts NC, AC, and ANC and the UV-vis absorbance spectra of Ag are plotted in Figure 5.4(a). The Ag spectrum exhibits two broad absorption peaks, located at 400 nm and 553 nm. The lower wavelength peak at 400 nm is interpreted to be primarily resulting from the plasmonic resonance effect associated with the spherical geometry of Ag nanoparticles, and another broader peak at 553 nm was associated with plasmonic resonances arising from Ag nanoparticles of various sizes and shapes, including triangular nanoplates, oblate structures, and irregular forms, as observed in the TEM images. The presence of plasmonic Ag in the ANC sample is evident from the distinct bump at 400 nm in the absorption spectrum, indicating its characteristic plasmonic resonance. Additionally, the NC spectra exhibit an increasing absorption trend with decreasing wavelength across the visible-to-UV spectrum (550-300 nm). Similarly, there is an increasingly higher absorption in ANC below 550 nm and beyond 300 nm towards the UV region. This similar absorption trend of NC and ANC can be attributed to their common LDH phase. The optical bandgaps of the catalysts were derived from the Tauc plot derived from the Kubelka-Munk function (equation (2.7)), as depicted in Figure 5.4(b) [24]. The bandgaps were noted as 3.14 eV for both NC and ANC, and 1.77 eV for AC. The obtained bandgap values of NC and ANC align with the calculated energy gap of NiO, as shown in Figure 5.5(c). The ANC spectrum, in Figure 5.4(b), reveals a distinct bump starting at around 2.7 eV with a peak maximum at 3.1 eV, implying the onset of significant absorption attributed to the surface plasmon resonance (SPR) of Ag nanoparticles. Although SPR in Ag does not create a true bandgap, it can influence the optical properties in a manner that may resemble bandgap behavior [25]. This phenomenon can be interpreted as the plasmonic resonance occurring in Ag when the incident light energy surpasses 2.7 eV, aligning with the broad absorption peak of Ag centered at approximately 400 nm (3.1 eV).

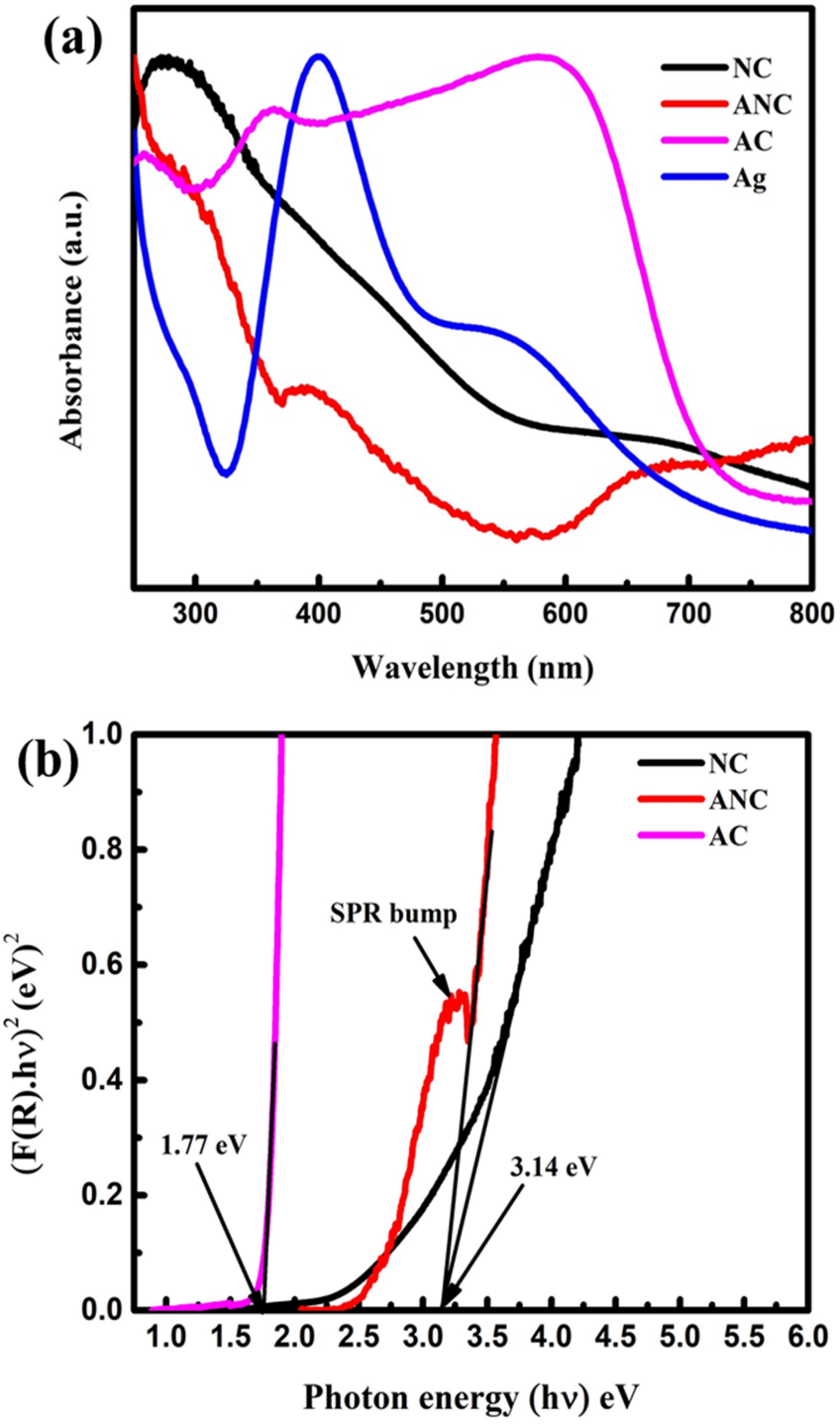

Figure 5.4. (a) UV-vis DRS of NC, AC, ANC, and UV-vis absorbance spectrum of Ag. (b) Bandgap determination using Tauc plot.

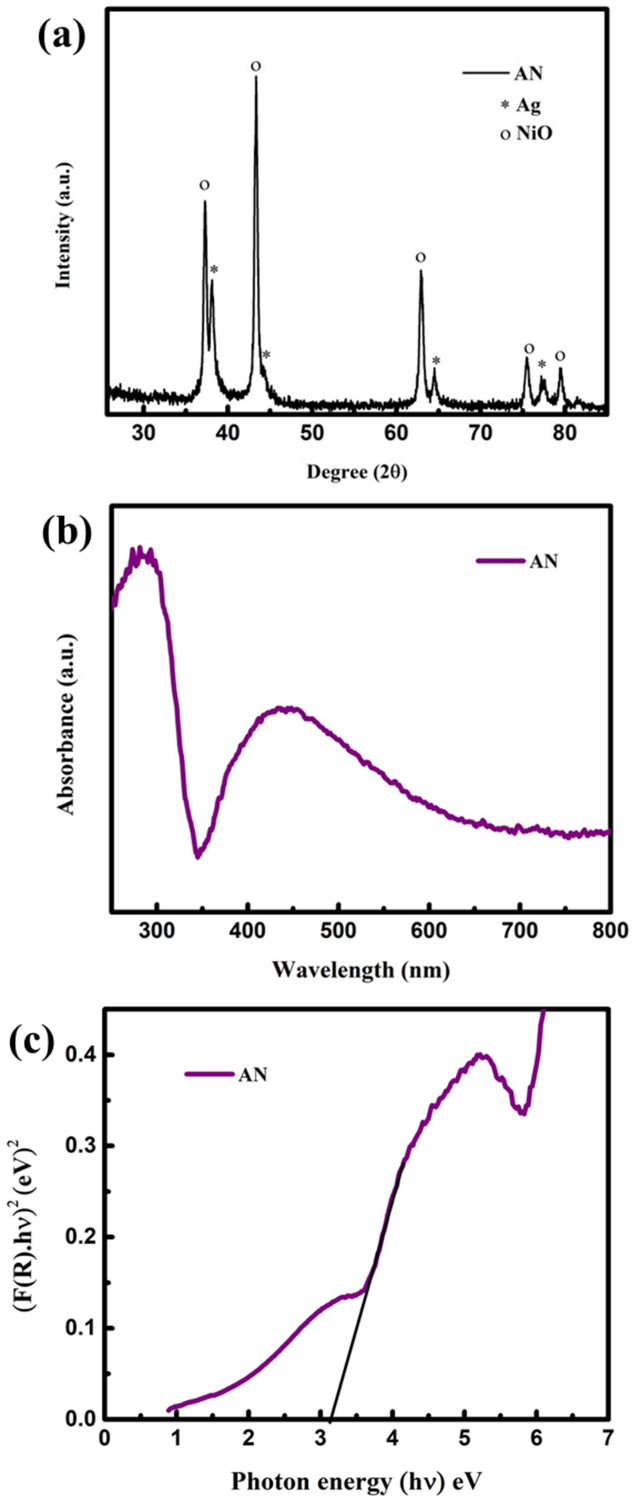

Figure 5.5. (a) X-ray diffraction spectra of AN (Ag@NiO), (b) UV-Visible DRS spectrum of AN, and (c) Bandgap determination of AN using Tauc plot.

5.3.2. Study of Raman and photoluminescence spectra

Figure 5.6(a) presents the Raman shift patterns of the photocatalysts NC, AC, and ANC. The peaks at 362, 598, and 798 cm^{-1} in the NC sample are clearly attributed to the formation of spinel $NiCr_2O_4$ [26-27]. Particularly, the intense and asymmetrical band (here with maxima at 798 cm^{-1}) is referenced to the symmetrical elongation vibration of the $[CrO_4]$ tetrahedron [28].

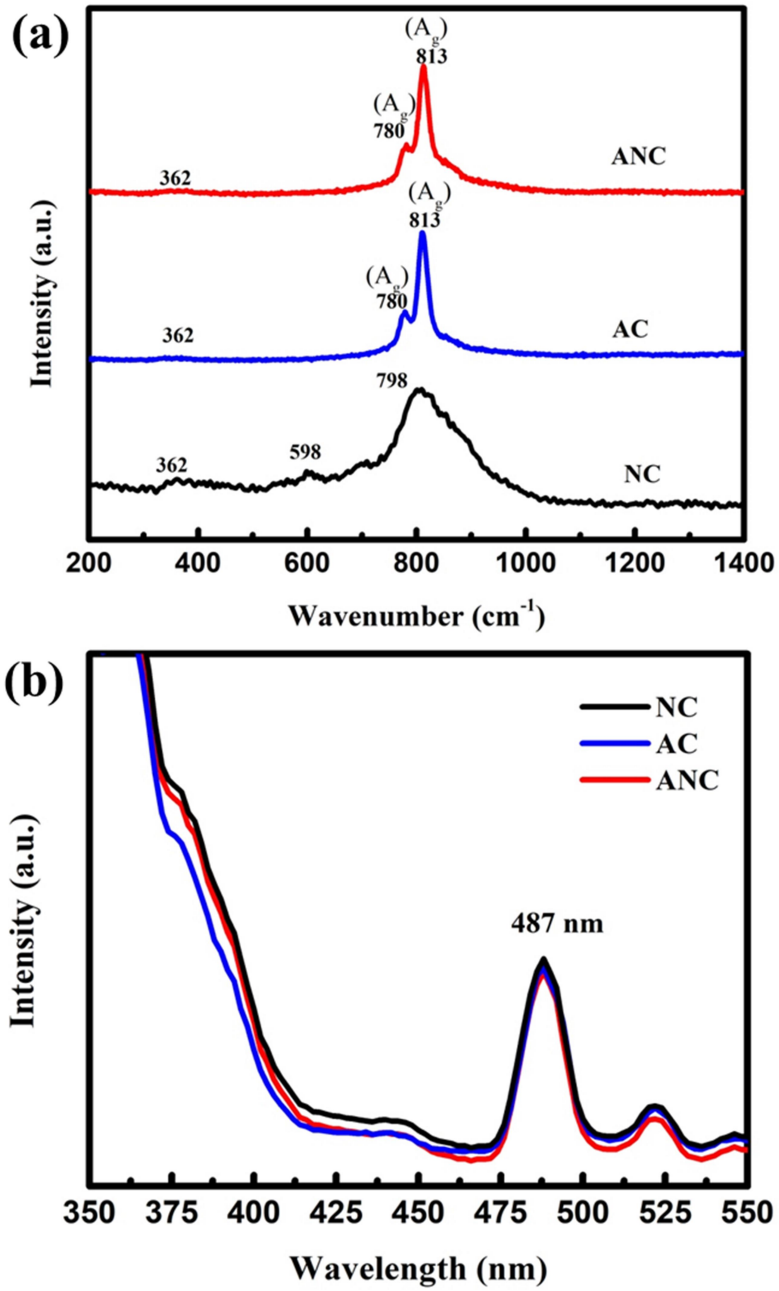

Figure 5.6. (a) Raman and (b) photoluminescence spectra of NC, AC, and ANC.

It has been explained that this anti-symmetrical elongation vibration is what contributes to the asymmetry of this band. The Raman spectra of ANC and pristine Ag_2CrO_4 (AC) exhibit nearly identical patterns. The strong peaks observed at 780 and 813 cm^{-1} are related to the symmetric stretching vibrations of the Cr-O bond in [CrO_4] clusters labeled as A_g mode [5, 29]. A small shift in the peak position from 816 cm^{-1} (reported in the literature) to 813 cm^{-1} may be due to the differences in synthesis method, crystallite size, defects in the lattice, and other factors [29]. All the samples (NC, AC, and ANC) have shown a common peak at 362 cm^{-1}, which can be attributed to Cr^{6+}, as all the samples contain Cr and O as their constituent elements [30].

The photoluminescence (PL) spectra of the catalysts NC, AC, and ANC were recorded under 325 nm excitation, as shown in Figure 5.6(b). All the photocatalysts displayed minimal emissions in the 400-550 nm wavelength range. Furthermore, ANC shows lower emission than both AC and NC within the wavelength range 450 nm to 550 nm as evidenced from Figure 5.6(b). The formation of a heterojunction between Ag_2CrO_4 and NiO in ANC, alongside a Schottky junction with metallic Ag, may lead to faster and higher electron-hole pair separation efficiency [31]. A peak at 487 nm is observed for both NC and ANC, which could be attributed to the NiO phase present in these samples [32-33]. Similarly, a peak at 487 nm is observed for AC caused by the recombination of charge carriers due to the defects in the structure of Ag_2CrO_4 [5].

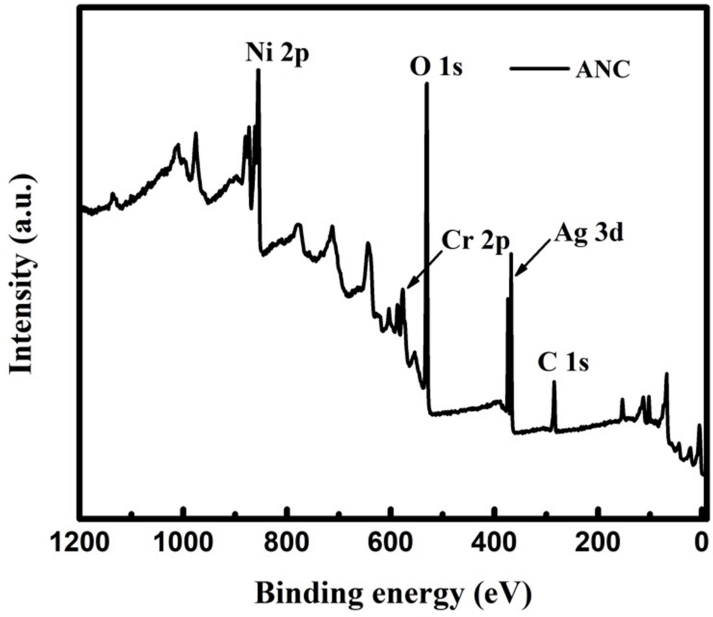

Figure 5.7. XPS spectra (full survey profile) of ANC.

5.3.3. XPS analysis

XPS technique was performed to investigate the elemental surface composition and electronic/oxidation states of the final ANC catalyst. Figure 5.7 shows the full survey spectrum of ANC in which Ni 2p, Cr 2p, O 1s, Ag 3d, and C 1s peaks were detected. The C signal observed at a binding energy value of 284.8 eV suggests the existence of the adventitious carbon on the sample [34].

The well-resolved Ni 2p spectrum of ANC is presented in Figure 5.8(a). The deconvolution of the Ni 2p spectrum results in six discrete peaks. The main peaks, located at 855.7 and 873.2 eV, are associated with Ni $2p_{3/2}$ and Ni $2p_{1/2}$ doublets, respectively, and are identified as the characteristic peaks of $Ni(OH)_2$ [35-37]. The difference in energy of these two peaks matches the spin-energy splitting value of 17.5 eV, characteristic of a $Ni(OH)_2$ phase [38]. The existence of $Ni(OH)_2$ is further confirmed by the peaks identified at 861.7 eV and 879.8 eV representing Ni $2p_{3/2}$ and Ni $2p_{1/2}$ satellite peaks of $Ni(OH)_2$, respectively [39].

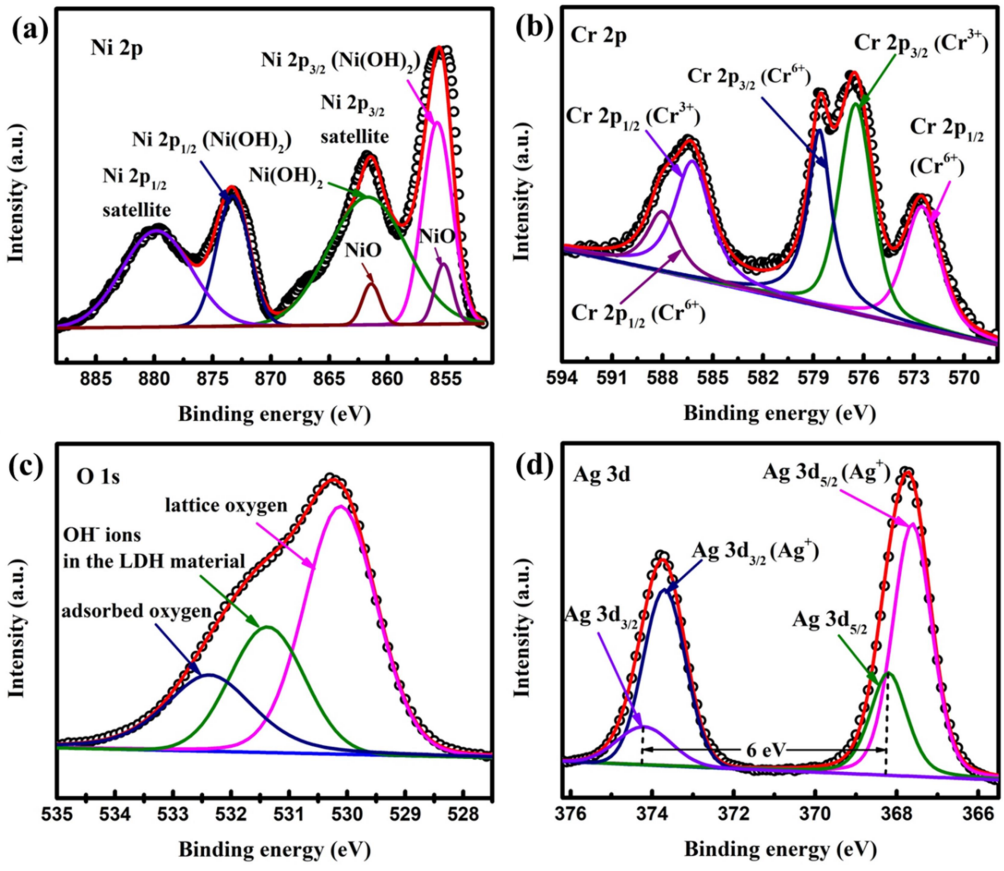

Figure 5.8. XPS peak fit of ANC: (a) Ni 2p spectra, (b) Cr 2p, (c) O 1s, and (d) Ag 3d.

While XRD analysis of the ANC material exclusively detected NiO crystalline phases, XPS revealed additional $Ni(OH)_2$ signatures. This can be attributed to the collapse of the LDH layered structure during calcination [18]. In this case, the interlayer anions and bonded hydroxyl molecules in ANC were completely removed after calcination. When exposed to water in the atmosphere and environmental anions, the LDH likely reformed its former stratified structure with new guest anions or hydroxyl ions, leading to the presence of $Ni(OH)_2$ [18]. Moreover, since XPS is a surface analysis technique, the $Ni(OH)_2$ peaks are found to be predominant [40]. As for the existence of NiO, two characteristic Ni $2p_{3/2}$ peaks at 855.2 eV and 861.4 eV are observed with a much smaller area, in agreement with XRD peaks [39]. In summary, analysis of the Ni 2p spectrum confirms only a single oxidation state, Ni^{2+}, present either as NiO or $Ni(OH)_2$.

Figure 5.8(b) depicts the core-level Cr 2p XPS measurement of ANC. The peak maxima recorded at 576.5 eV and 586.2 eV are associated with Cr^{3+} [21, 41-45]. The finding of Cr^{3+} agrees with the general formula of Ni-Cr LDH, in which one metal, Ni, is in a +2 oxidation state and the other metal, Cr, is in a +3 oxidation state. However, the XRD of ANC also revealed the presence of the Ag_2CrO_4 phase, where Cr is in the +6 oxidation state. This is further confirmed by the resolved peaks at 578.6 eV and 588.0 eV in the Cr 2p spectra, corresponding to Cr^{6+} [46-48]. The additional peak identified at 572.5 eV originates from the interaction between Ag 3p and Cr 2p and is referenced as the Ag $3p_{3/2}$ peak [49, 50]. The O1s spectra as provided in Figure 5.8(c) could be resolved into three distinct peaks positioned at 530.1 eV, 531.4 eV, and 532.3 eV, which implies the lattice oxygen (Ni-O or Cr-O), hydroxyl oxygen (OH^- ions in the LDH material), and adsorbed oxygen, respectively [35, 39, 41, 44, 51]. Again, the high-detailed XPS binding energy spectrum of Ag 3d of the ANC photocatalyst is shown in Figure 5.8(d). The deconvoluted XPS peaks at 367.6 eV and 373.6 eV are associated with the oxidation state of Ag as Ag^+, which supports the formtion of Ag_2CrO_4 as revealed in XRD and Cr 2p peaks [46, 48, 52]. Moreover, the fitted XPS peaks maxima at 368.2 eV ($3d_{5/2}$) and 374.2 eV ($3d_{3/2}$) correspond to the Ag 3d doublet caused by the spin-orbit splitting, with a binding energy difference of 6.0 eV between them, indicating the metallic form of Ag [53-55].

To ascertain the energy band extremities values of the ANC catalyst, the valence band XPS spectra were analyzed as depicted in Figure 5.9. Extrapolation at the onset of

the spectra, as given in Figure 5.10, reveals a valence band maximum (VBM) of 1.26 eV.

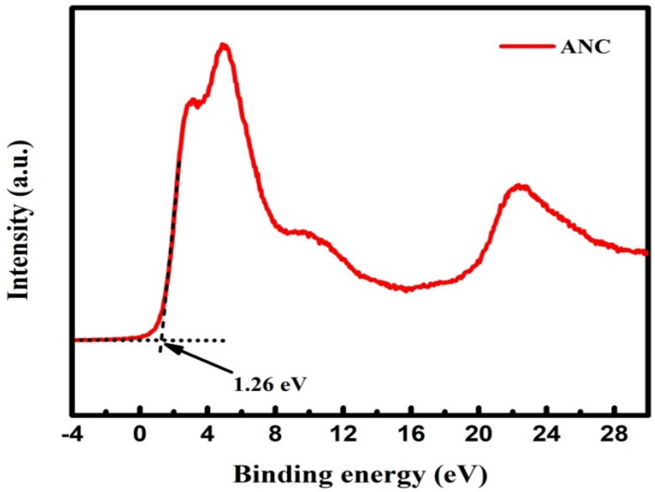

Figure 5.9. Valence band XPS spectra of ANC.

5.3.4. SEM and TEM Analysis

The SEM images of NC exhibit a highly aggregated, porous morphology with nanoparticle clusters forming interconnected structures, shown in Figure 5.10(a-b).

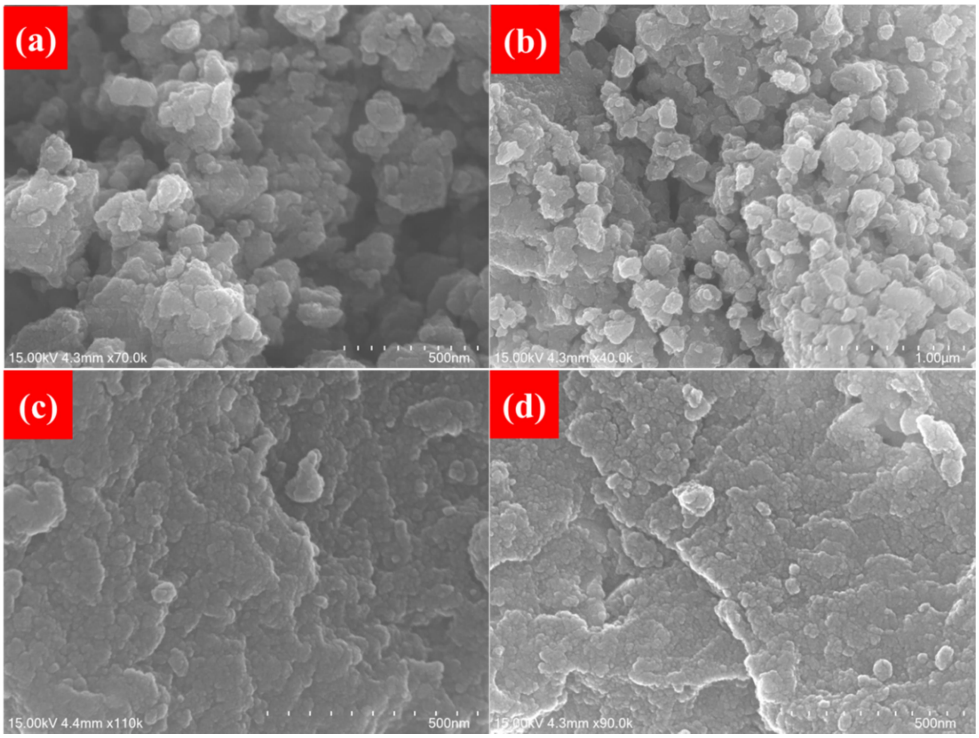

Figure 5.10. SEM images of (a-b) NC and (c-d) ANC.

While a distinct layer-by-layer arrangement is not explicitly visible, the observed agglomerates and rough texture suggest the possible retention of interlayer porosity, a characteristic feature of LDH-derived materials. This porous architecture may result in a high surface area, which can enhance dye adsorption, offering substantial active sites for photocatalytic reactions. In contrast, ANC, as shown in Figure 5.10(c-d) displays fused layers, implying that the formation and growth of Ag_2CrO_4 have bridged gaps and reduced the height disparity between the uppermost and lowermost surfaces. The stacked and textured appearance observed in the SEM image suggests the presence of residual LDH structures, indicating the retention of its layered morphology in the ANC composite.

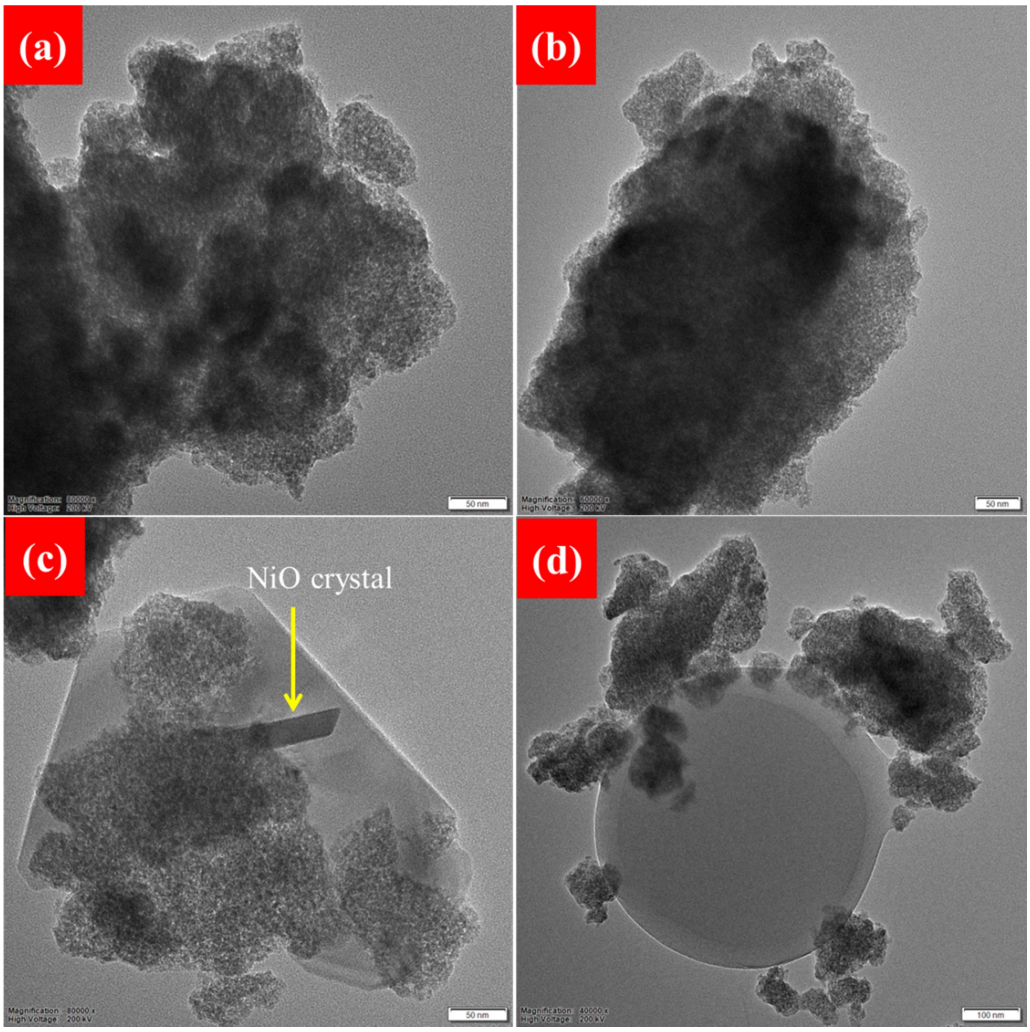

Figure 5.11. (a-d) TEM images of NC.

To obtain detailed information on the morphology of the catalyst, TEM images were investigated. The TEM images of NC, shown in Figure 5.11(a-d), provide a more comprehensive view of the material's structure. In addition to confirming the layered arrangements, the images reveal a mesoporous structure, as observed in Figure 5.11(a-b). The TEM image in Figure 5.11(c) displays a distinct rod-shaped crystal, identified as NiO [56]. Furthermore, Figure 5.11(d) indicates that NC forms a circular structure, which appears to be encapsulated and wrapped with particles, forming the structures shown in Figure 5.11(a-c).

The TEM pictures and SAED pattern of ANC are shown in Figure 5.12(a-c) and Figure 5.12(d), respectively.

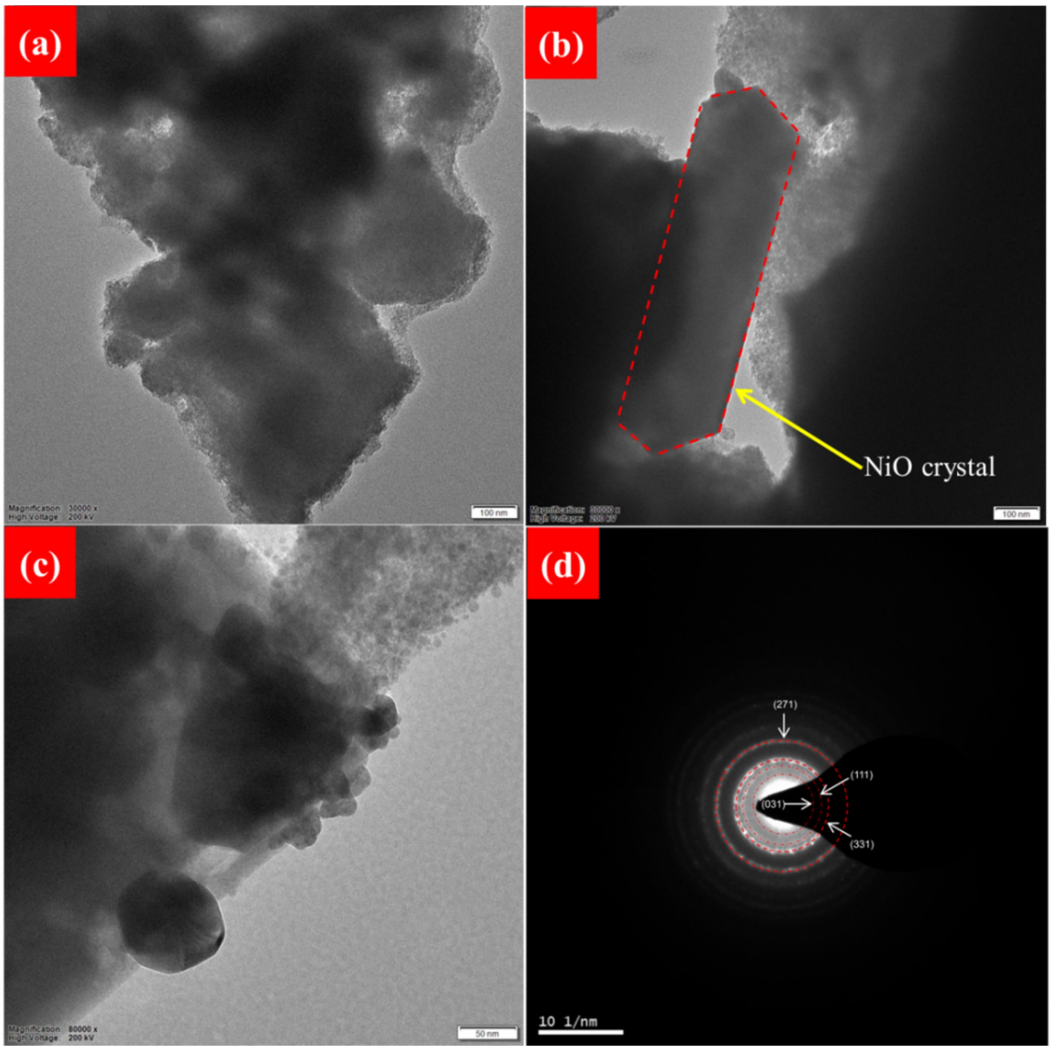

Figure 5.12. TEM images of (a-c) ANC, and (d) SAED pattern of ANC.

It is apparent that ANC is a less porous material with increased crystallinity. Faceted NiO crystal and spherical Ag_2CrO_4 crystals are visible in Figures 5.12 (b) and (c), respectively [5, 56].

The measurement of the radius of concentric circles (highlighted with the red color dotted curve) of the SAED pattern image in Figure 5.12(d) reveals four different interplanar spacings of values 0.28, 0.21, 0.18, and 0.13 nm, which are assigned to planes (031), (111), (331), and (271), respectively. The planes (031), (331), and (271) correspond to the growth planes of Ag_2CrO_4 in three different directions, while (111) corresponds to the crystal plane of Ag. High-resolution TEM images of ANC are presented in Figure 5.13(a-b). The measurements of interplanar distances confirm the presence of three distinct phases in ANC, which are Ag, NiO, and Ag_2CrO_4.

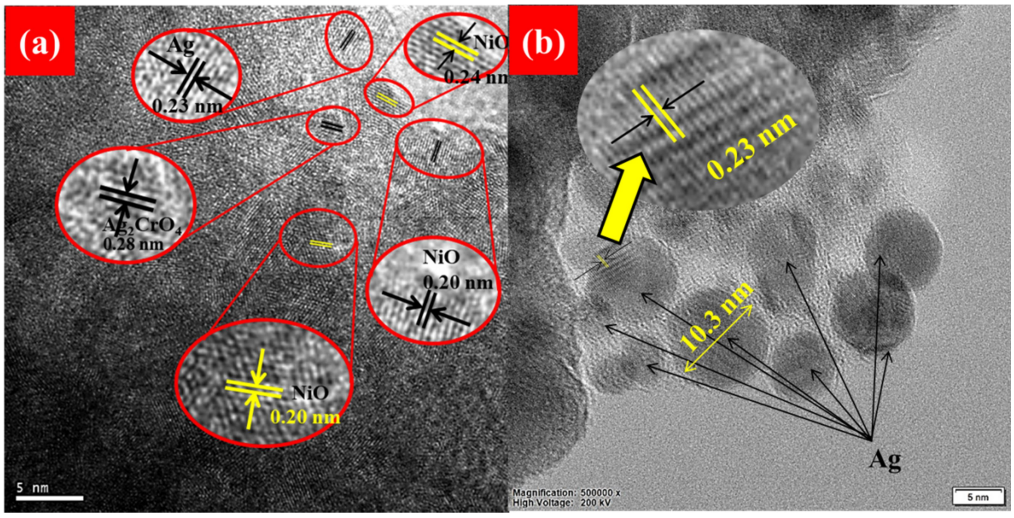

Figure 5.13. (a-b) High resolution-TEM images of ANC.

From the HR-TEM images, in Figure 5.13(a), two distinct spacings of NiO are identified at d = 0.24 nm and 0.20 nm, corresponding to the (222) and (400) planes, respectively. In addition, Ag_2CrO_4 exhibits an interplanar spacing of d = 0.28 nm corresponding to the (031) plane, while metallic Ag shows a spacing of d = 0.23 nm corresponding to the (111) plane. Figure 5.13(b) further shows distinct spherical Ag nanoparticles of various sizes between the 5-11 nm range. TEM images of Ag that were used to prepare ANC, are presented in Figure 5.14(a-d). The EDX analysis of both NC and ANC provides further confirmation of the elemental composition of these materials. The analysis, as shown in Figure 5.15, highlights the presence of constituent elements,

verifying the successful incorporation of the desired components within the synthesized samples.

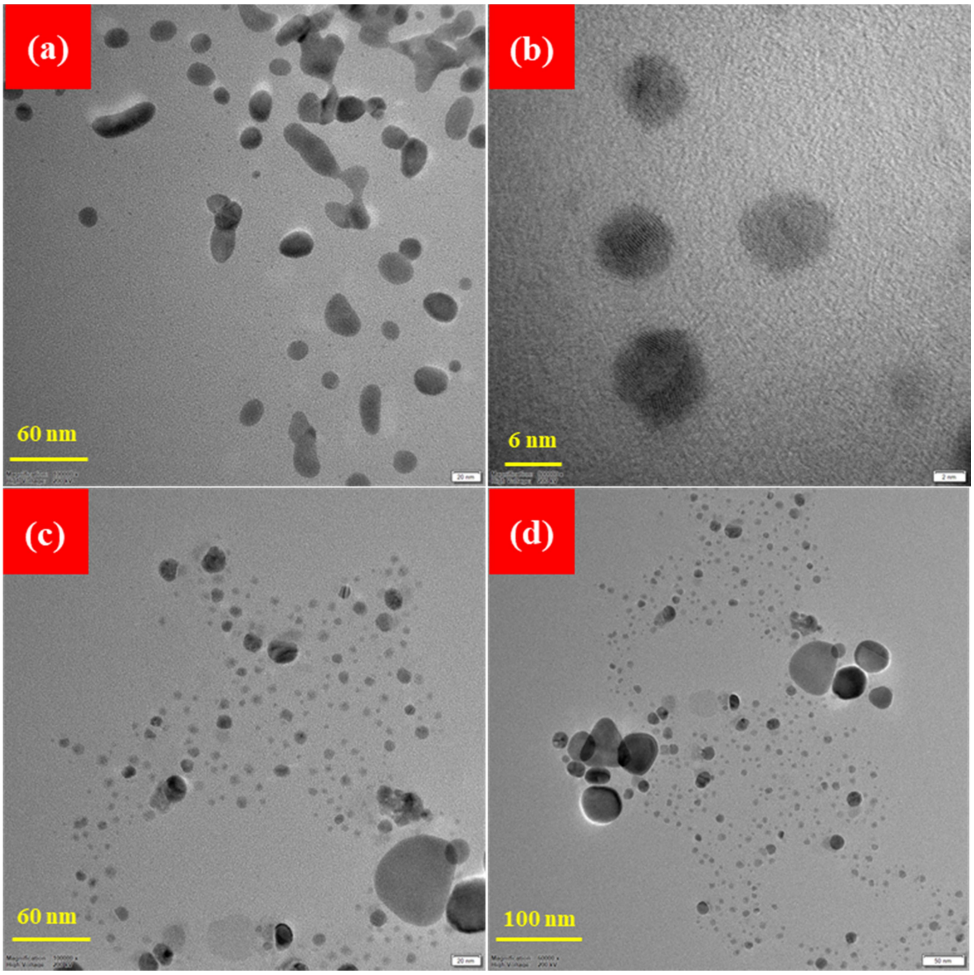

Figure 5.14. (a-d) TEM images of Ag nanoparticles (at different magnifications).

5.3.5. Photocatalytic activity test

The photocatalytic ability of the photocatalysts was determined by tracking the degradation of MB and RhB. Figure 5.16(a) demonstrates the degradation trend of MB under exposure to visible light for a duration of 90 minutes. The degradation percentage from highest to lowest follows the sequence: ANC > AC > NC, with values of 94.6%, 88.3%, and 11%, respectively. The absorption spectra of MB recorded at different moments of time using the photocatalysts and the photographic representation of MB degradation, captured at 15-minute intervals during irradiation, is displayed in Figure 5.17(a-c) and 5.18, respectively.

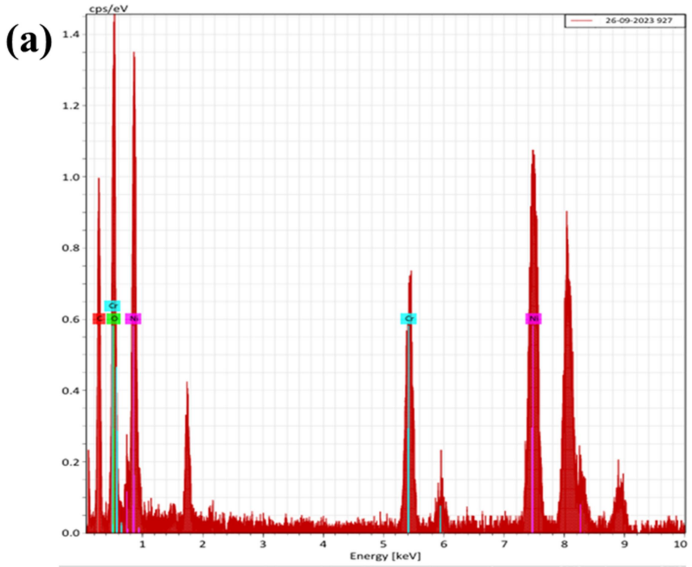

Element	At. No.	Netto	Mass [%]	Mass Norm. [%]	Atom [%]	abs. error [%] (1 sigma)	rel. error [%] (1 sigma)
Carbon	6	1395	24.658	24.658	46.170	1.017	4.123
Oxygen	8	2295	23.540	23.540	33.088	0.885	3.761
Chromium	24	2825	18.110	18.110	7.833	0.678	3.745
Nickel	28	4279	33.693	33.693	12.910	1.176	3.489
		Sum	**100.000**	**100.000**	**100.000**		

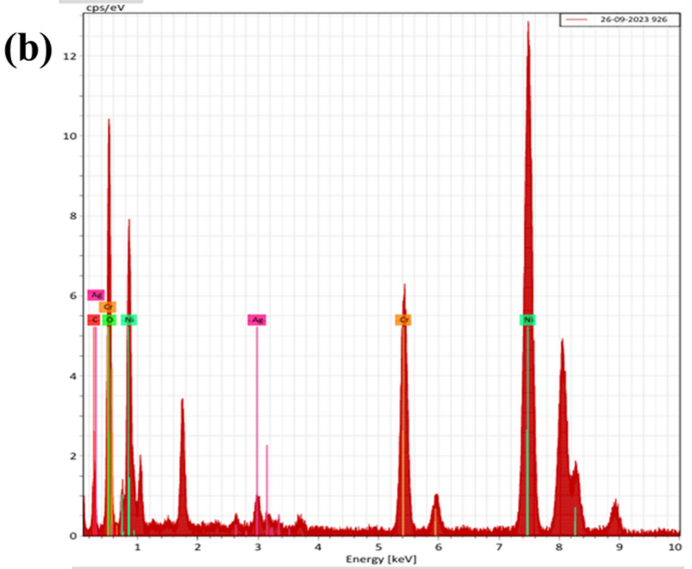

Element	At. No.	Netto	Mass [%]	Mass Norm. [%]	Atom [%]	abs. error [%] (1 sigma)	rel. error [%] (1 sigma)
Carbon	6	1760	3.706	3.706	10.748	0.167	4.506
Oxygen	8	16401	20.037	20.037	43.627	0.646	3.225
Chromium	24	25481	19.455	19.455	13.034	0.623	3.202
Nickel	28	56149	52.659	52.659	31.254	1.622	3.081
Silver	47	3441	4.143	4.143	1.338	0.449	10.827
		Sum	**100.000**	**100.000**	**100.000**		

Figure 5.15. EDX plot of (a) NC and (b) ANC photocatalysts along with the table showing the atomic composition and percentage.

The rate constants were calculated as 0.034, 0.025, and 0.001 min^{-1} for ANC, AC, and NC, respectively, from the graph of ln C/ C_o versus time, as shown in Figure 5.16(b). The degradation was in accordance with pseudo-first-order kinetics, exhibiting a high R^2 value (0.98, 0.99, 0.86). The degradation rate obtained for the ANC photocatalyst is 34 times higher than the pristine NC. The retention of the lamellar LDH structure in ANC, as evidenced by SEM images and XPS spectra, even after forming the heterojunction between NiO and Ag_2CrO_4, offers abundant active sites and facilitates efficient charge carrier separation.

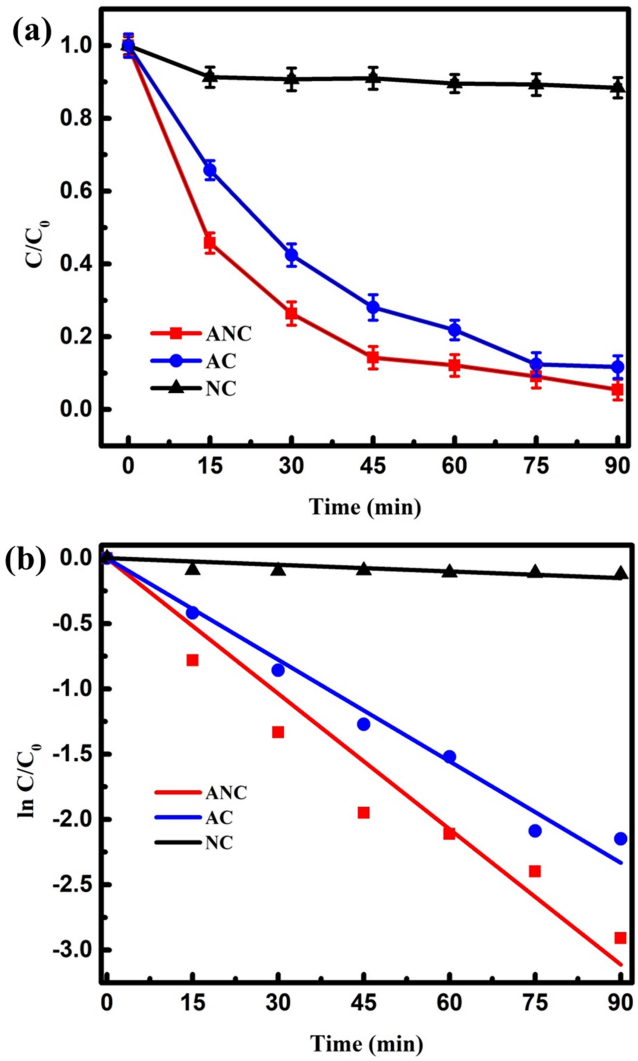

Figure 5.16. (a) Photocatalytic degradation pattern (C/C_o vs. time) of MB upon visible light exposure (0 to 90 min) using NC, AC, and ANC photocatalyst, (b) ln C/C_o against time plot to determine the rate constant.

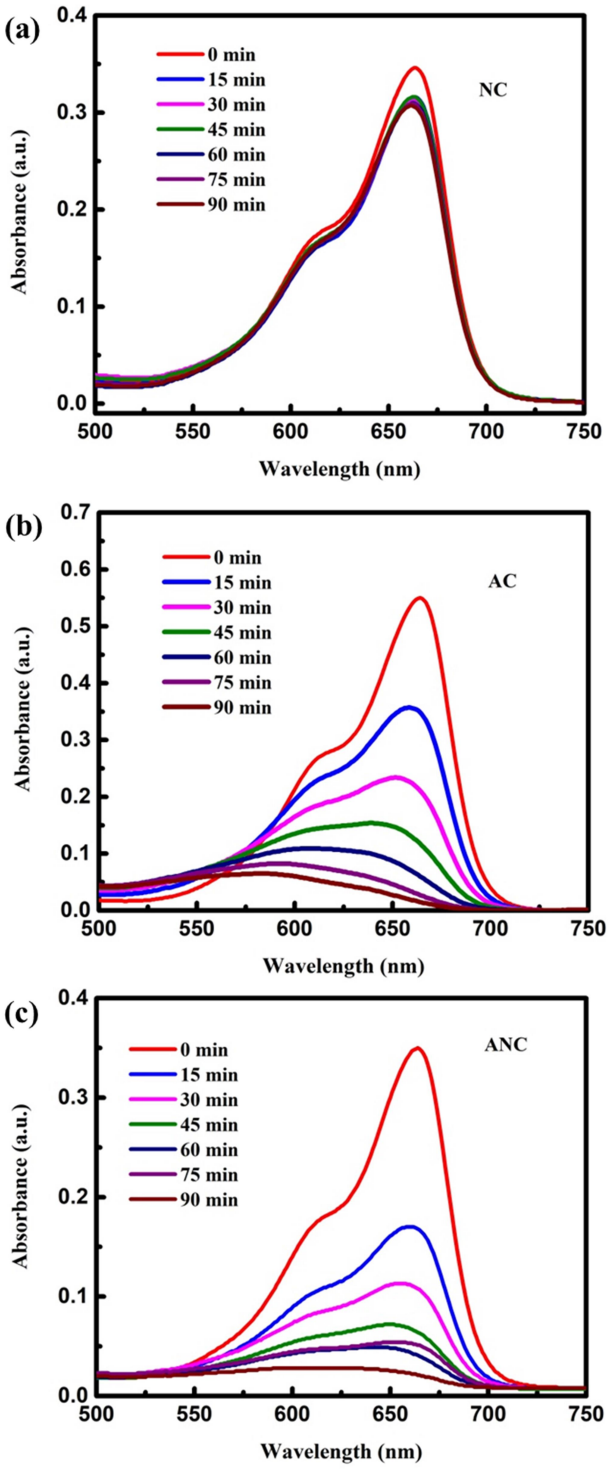

Figure 5.17. Absorption spectra of MB recorded for a total duration of 90 min light irradiation in the presence of (a) NC, (b) AC, and (c) ANC photocatalysts.

Furthermore, $Ni(OH)_2$, with its strong electronegativity, suppresses photogenerated carrier recombination, while combining NiO with $Ni(OH)_2$ enhances the separation of photo-stimulated charge carriers and generates active species for photocatalytic reactions [57]. The Ag_2CrO_4 catalyst also demonstrates effective MB degradation on its own, attributed to strong absorption of visible light and efficient generation of charge carriers [58]. Additionally, Ag nanoparticles in metallic form act as a plasmonic sensitizer, which broadens the light response of the semiconductors. With the establishment of a Schottky barrier between metallic Ag nanoparticles and semiconductor domains, electrons seamlessly transfer from Ag, which serves as both an electron reservoir and a catalytic centre.

Figure 5.18. Photographic representation of MB degradation, captured at 15-minute intervals during visible-light irradiation of the MB solution containing the ANC photocatalyst, from 0 to 90 minutes.

Table 5.1. Rate constant and regression coefficient for MB degradation.

Photocatalysts	Rate constant (min^{-1})	Regression coefficient
NC	0.001	0.86
AC	0.025	0.99
ANC	0.034	0.98

This process accelerates electron migration while effectively suppressing carrier recombination, thereby enhancing charge separation efficiency. Table 5.1 shows the rate constants for MB degradation of all the photocatalysts along with their regression coefficients from the linear fitting. Additionally, rhodamine B (RhB) degradation was performed with the photocatalysts under identical experimental conditions and light exposure. The degradation spectra of RhB are displayed in Figure 5.19(a-b).

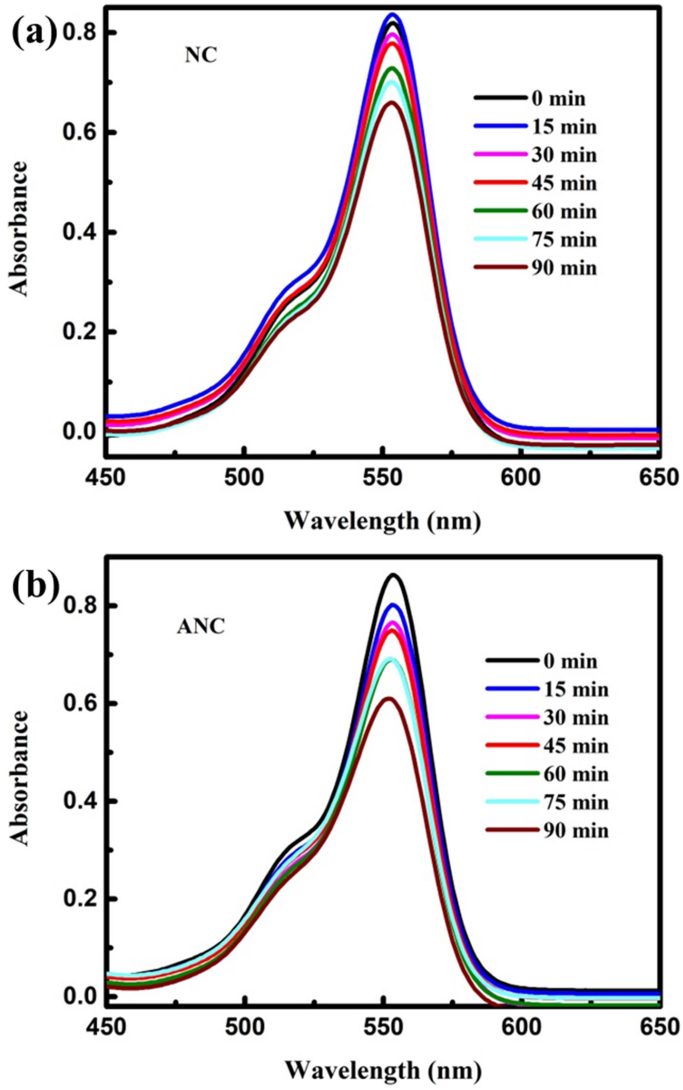

Figure 5.19. Absorption spectra of RhB recorded for a total duration of 90 min light irradiation in the presence of (a) NC and (b) ANC photocatalysts.

The analysis demonstrated that the ANC photocatalyst demonstrated 1.4 times greater activity than NC. The weaker performance of ANC in terms of RhB degradation

(Figure 5.20) could be inferred from the role of radicals in RhB degradation. RhB is a dye molecule of molecular weight 479.01 g/mol, which is larger compared to that of MB (319.85 g/ mol) [59, 60].

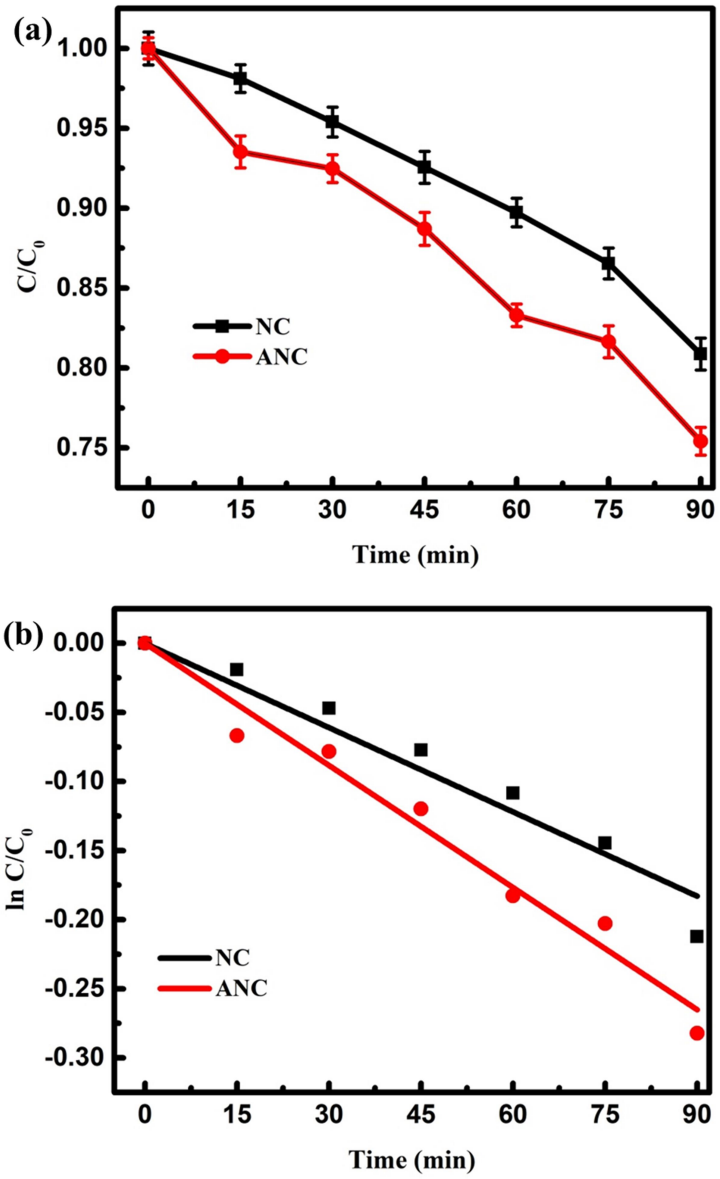

Figure 5.20. (a) Photocatalytic degradation pattern (C/C_o vs. time) of RhB upon visible light exposure using NC and ANC photocatalyst, (b) ln C/C_o vs. time graph.

The degradation mechanism of RhB has been widely studied, and it is accepted that both h^+ and •OH hold a crucial role in enhancing the breakdown of RhB molecules [61, 62]. At the first stage of degradation, two competitive processes are said to occur

simultaneously, namely N-deethylation and chromophore cleavage [62, 63]. The cleavage is an important step towards full degradation of RhB, whereby it is converted to CO_2 and H_2O. The radicals that are mainly responsible for this cleavage have been identified as h^+ and •OH [61, 62]. The •OH that can be obtained from the oxidation of H_2O molecules by h^+ requires a redox potential of 2.3 eV [64, 65] which is not probable according to the band edge potentials of ANC proposed in this study. However, the production of •OH in the ANC photocatalytic system could occur from the participation of electrons in various oxidation reactions via oxygen and water molecules [64]. But accordingly, the population of •OH would be less abundant and thus account for a slower degradation rate. For MB, the electrons and singlet oxygen are capable enough to degrade MB and thus faster degradation for MB [66]. Furthermore, the reusability test of MB degradation using ANC photocatalyst, was performed under the similar experimental set-up for three consecutive cycles as shown in Figure 5.21. The total MB removal percentages achieved in three consecutive cycles are 97%, 81% , and 68%, respectively.

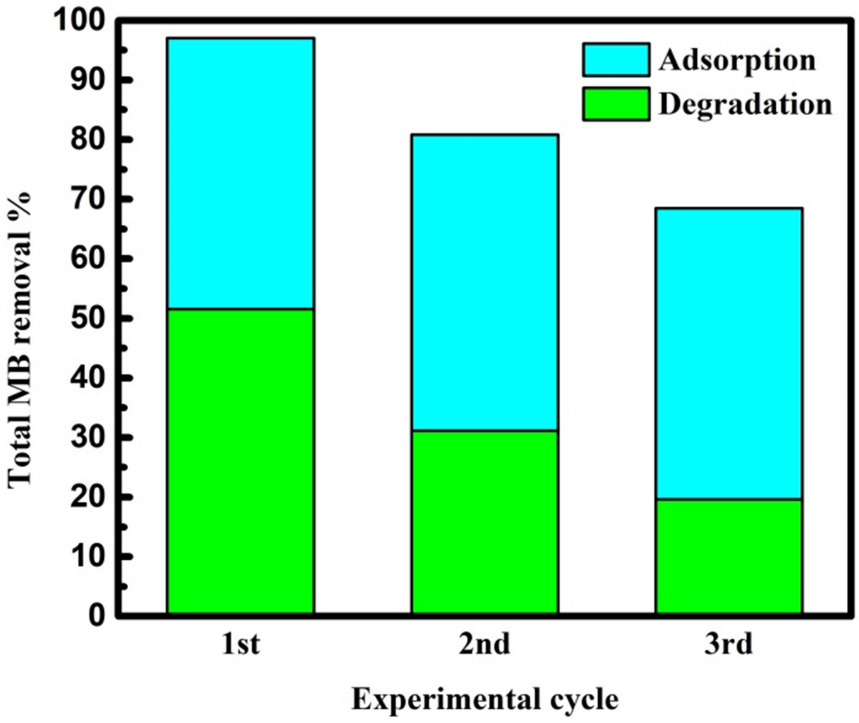

Figure 5.21. MB removal efficiency of the ANC photocatalyst over three consecutive photocatalytic cycles.

5.3.6. Scavenger-based radical identification experiments

To examine the participating active species and their degree of influence in the degradation of MB using the ANC photocatalyst, free radical quenching experiments were conducted. It is known that the photocatalytic process proceeds via the major reactions as outlined in Eq. (1.1-1.9) in Chapter 1. Figure 5.22(a) shows the degradation of MB using different quenching agents over the course of 90 minutes.

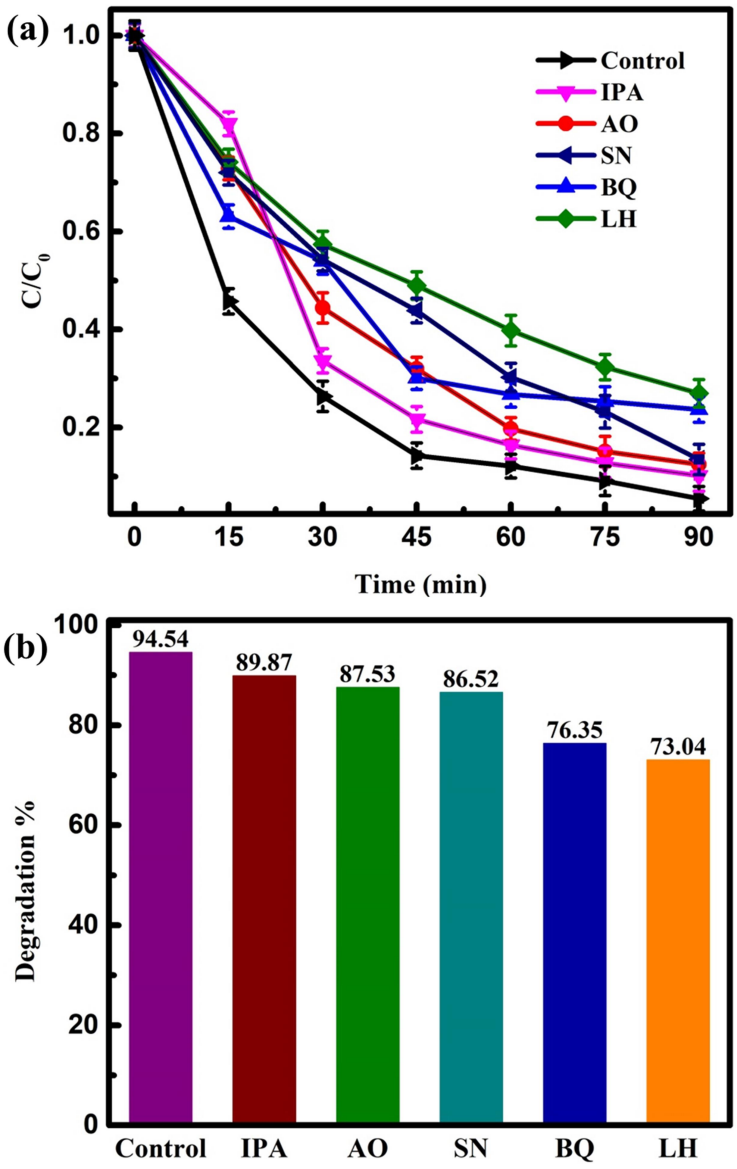

Figure 5.22. (a) MB degradation over time and (b) degradation efficiency (%), achieved by the ANC photocatalyst in the presence of different scavenging agents.

It was found that the addition of LH ($^1O_2$ quencher) to the MB solution, lowered the degradation ability of the photocatalyst to a maximum degree in comparison to all other quenching agents tested [67]. The degradation percentages of MB after the addition of specific quenching agents are shown in Figure 5.22(b). Experimental observations indicated that the presence of BQ ($\bullet O_2^-$ quencher) and SN (e^- quencher) in the MB solution produced the second and third-highest reduction in degradation efficiency, respectively. This observation suggests that electrons (e^-) play a more significant role than holes (h^+) in the degradation of MB using the ANC photocatalyst. This can be explained by the reaction pathways described in Eq. (1.2) and (1.9), where e^- reduces O_2 to produce $\bullet O_2^-$, and $\bullet O_2^-$ subsequently interacts with h^+ to generate $^1O_2$ [67, 68]. Therefore, when e^- is quenched, $\bullet O_2^-$ production is hindered, and the reduced $\bullet O_2^-$ level impairs the generation of $^1O_2$ species, which is the primary reactive species responsible for MB degradation in the ANC photocatalyst system. In contrast, the addition of AO (h^+ quencher) and IPA (•OH quencher) had a minimal effect on MB degradation as shown in Figure 5.22(b).

5.3.7. Mott-Schottky analysis

To explore the potential photocatalytic mechanism of the ANC (Ag@NiO/Ag_2CrO_4 heterojunction), its flat band potential was determined as shown in Figure 5.23. The results show that NiO is a p-type semiconductor with E_{fb} = 1.7 eV vs Ag/AgCl, whereas AC and ANC are showing an n-type conductivity with E_{fb} = 0.34 eV and 0.35 eV vs Ag/AgCl, respectively. The equivalent flat band energies (E_{fb} vs NHE) of NiO, AC, and ANC are therefore ~1.92 eV, ~0.56 eV, and ~0.57 eV, respectively, using the formula $E_{NHE} = E_{Ag/AgCl} + 0.222$ eV [69]. Since, the valence band maximum and conduction band minimum vary by 0.1 eV from the flat band potentials, therefore, the band edge positions (E vs NHE) of NiO (E_V), AC (E_C) and ANC (E_C) are obtained at around ~2.02 eV, ~0.46 eV and ~0.47 eV, respectively [70, 71].

5.3.8. Photocatalytic mechanism

The photocatalytic mechanism of the ANC photocatalyst, illustrated in Figure 5.24, is proposed based on data obtained from UV-visible spectroscopy, UV-DRS, Tauc plots, active radical quenching experiments, and band edge positions derived from the Mott-Schottky plot. The ANC composite consists of NiO and Ag_2CrO_4, as determined by

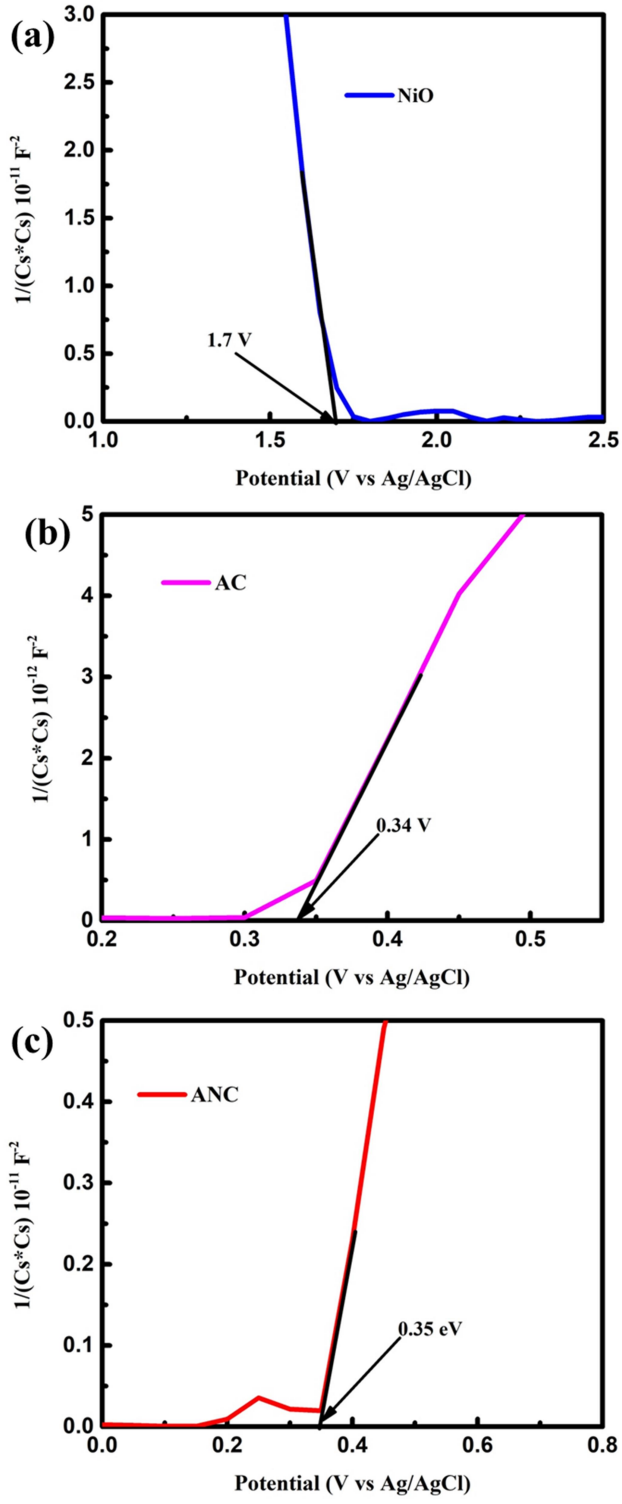

Figure 5.23. Mott–Schottky plots of counterparts (a) NiO, (b) AC, and composite (c) ANC.

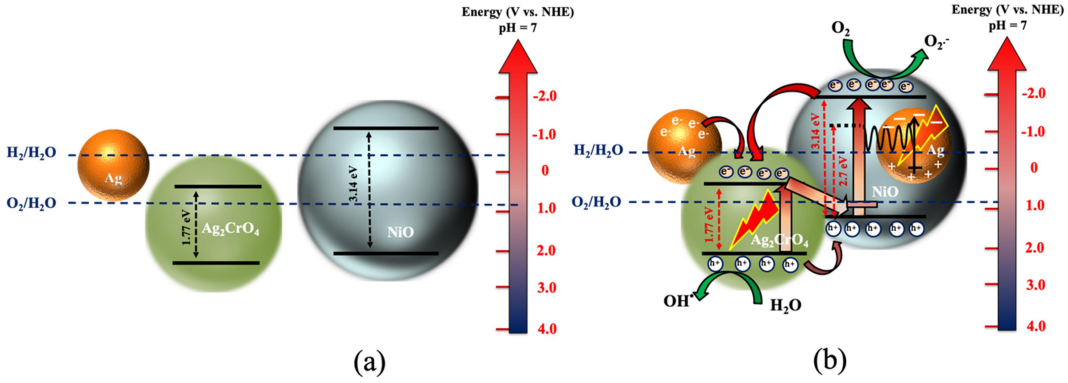

Figure 5.24. Proposed photocatalytic mechanism of ANC photocatalyst (a) before and (b) after heterojunction. A p-n heterojunction with Z-scheme charge transfer dynamics, facilitated by plasmonic Ag via the PIRET mechanism.

XRD and XPS spectral analysis. Consequently, the ANC composite features a heterojunction system formed between NiO and Ag_2CrO_4. Furthermore, bandgap calculations based on Tauc plots reveal values of 1.77 eV for AC and 3.14 eV for ANC, where the 1.77 eV bandgap corresponds to Ag_2CrO_4 and the 3.14 eV bandgap to NiO. The valence band maximum (VBM) of NiO, determined from the Mott-Schottky plot, was found to be around 2.02 eV (V vs. NHE, shown in Figure 5.24). Similarly, the conduction band minimum (CBM) of AC (Ag_2CrO_4) and ANC was calculated as approximately 0.46 eV and 0.47 eV, respectively. The nearly identical CBM values for AC and ANC indicate that the band edge positions of Ag_2CrO_4 in ANC remain unchanged. Consequently, the band edge positions of Ag_2CrO_4 in ANC are considered to be 0.47 eV (CBM) and 2.24 eV (VBM), amounting to a bandgap of 1.77 eV. The band edge positions of NiO before heterojunction are calculated to be -1.12 eV (CBM) and 2.02 eV (VBM), accounting for a bandgap of 3.14 eV. This suggests the development of a p-n heterojunction between NiO and Ag_2CrO_4. Furthermore, the VBM of ANC was found to be 1.26 eV from the VB XPS spectrum, which is equivalent to 1.32 eV vs NHE using the formula [72]: $E_{NHE} = \phi + E_{VB\ (XPS)} - 4.44\ eV$, where E_{NHE} refers to the potential of standard hydrogen electrode, ϕ represents the work function associated with the XPS spectrometer (4.5 eV for the instrument used), and $E_{VB(XPS)}$ is the VBM in eV, obtained from VB XPS spectrum. This can be interpreted as the energy corresponding to the outermost valence electron in the ANC photocatalyst and resulting

from the band bending effect, positioned 0.7 eV above the VBM of NiO (2.02 eV) after heterojunction [73]. The determined band edge alignments before and after the heterojunction are shown in Figure 5.24(a-b). With the incorporation of Ag nanoparticles (with the Fermi energy at 0.3 eV), a Schottky junction can be effectively formed with NiO, exhibiting rectifying behavior due to the higher Fermi level of Ag relative to p-type NiO [74]. In contrast, Ag forms an Ohmic contact with AC, as its Fermi level is more negative (in potential vs NHE) than that of n-type AC, illustrated in Figure 5.24. The photocatalytic mechanism can be understood as follows: When visible light with an energy of 1.77 eV or higher is incident on the photocatalyst, electrons in Ag_2CrO_4 are excited across the bandgap from the valence band (VB) to the conduction band (CB). These excited electrons subsequently relax to the VB of NiO. Furthermore, upon exposure to visible light with an energy of 2.7 eV or higher, Ag nanoparticle hosts localized surface plasmon resonance (LSPR), generating highly energetic electrons, as confirmed by plasmonic absorption spectra [75]. Subsequently, electrons situated in the VB of NiO can be further excited to its conduction band (CB) through plasmon-induced resonant energy transfer (PIRET), facilitated by dipole-dipole coupling between Ag nanoparticles and the NiO semiconductor. The occurrence of PIRET in ANC is supported by the overlapping of LSPR band spectra of Ag with the bandgap absorption of NiO at around 400 nm (3.1 eV). Through nonradiative relaxation of localized surface plasmon dipoles, resonant energy transfer (RET) can effectively generate electron-hole pairs within the semiconductor. Unlike direct optical excitation, RET facilitates the generation of charge carriers at energies within and outside the bandgap region by transferring energy into near-the-band-edge states that are typically not optically active [76, 77]. Furthermore, the Schottky barrier developed at the Ag-NiO interface ensures unidirectional electron transfer into NiO, either through RET or direct electron injection, thereby facilitating their availability for chemical reactions [78]. The occurrence of RET is further supported by the results of active radical quenching experiments, where $^1O_2$, $\bullet O_2^-$, and e^- significantly influence the photocatalytic process in the order $^1O_2 > \bullet O_2^- > e^-$. The contribution of electrons to the photocatalytic process is expected to be minimal, as electrons from the CB of NiO can transfer to the CB of Ag_2CrO_4, where the energy level is insufficient to drive the reduction of O_2 to $\bullet O_2^-$. However, RET facilitates the continuous regeneration of electron-hole pairs in NiO,

even after electrons from the CB of Ag_2CrO_4 relax to the VB of NiO. This process sustains a Z-scheme mechanism under visible light illumination. The electrons excited in the CB of NiO subsequently reduce O_2 to $\bullet O_2^-$, which actively targets and degrades MB dye molecules [79]. Moreover, when $\bullet O_2^-$ species interact with the energetic holes residing at the VB of Ag_2CrO_4, they produce $^1O_2$, which further enhances the degradation of dye molecules. Besides, the photocatalyst can also produce other reactive oxygen species (ROS), such as H_2O_2 and •OH, in the presence of atmospheric oxygen within the reactor system [80-82]. These active ROS target the dye molecules, breaking them into simpler compounds. The end products, formed through a series of reactions between the charged species and intermediates generated from the initial degradation of dye molecules, are CO_2 and H_2O [81]. It may be highlighted that the photoexcited holes after relaxing from the VB of Ag_2CrO_4 to the VB of NiO (VBM = 2.02 eV) lack the necessary potential to generate •OH radicals from water molecules, as this reaction requires an energy of at least 2.3 eV [64]. This finding is further supported by active radical quenching experiments, where the suppression of •OH radicals had the least significant impact on photocatalysis. However, since Ag_2CrO_4 alone can facilitate photocatalytic degradation, shown in Figure 5.16(a), the energetic holes situated at the VB must play a crucial role in generating •OH radicals, as its VBM lies at around 2.24 eV. This is particularly significant, as the conduction band edge of Ag_2CrO_4 is energetically not favorable for the reduction of O_2 to $\bullet O_2^-$.

Furthermore, the charge transfer behaviour of NC, AC, and ANC is compared using time-resolved photoluminescence spectra (TRPL) measurements as shown in Figure 5.25. The TRPL decay profiles of NC and AC were well described by a single-exponential function, yielding one characteristic lifetime (τ), whereas three different time constants (τ) were found for ANC, indicative of multiple recombination and interfacial relaxation pathways. The corresponding values of the time constants are given in the inset of Figure 5.25, along with the average lifetime value calculated for ANC. The average exciton lifetimes for NC and AC are 0.83 ns and 0.82 ns, respectively, whereas ANC exhibits a significantly longer value of 1.43 ns.

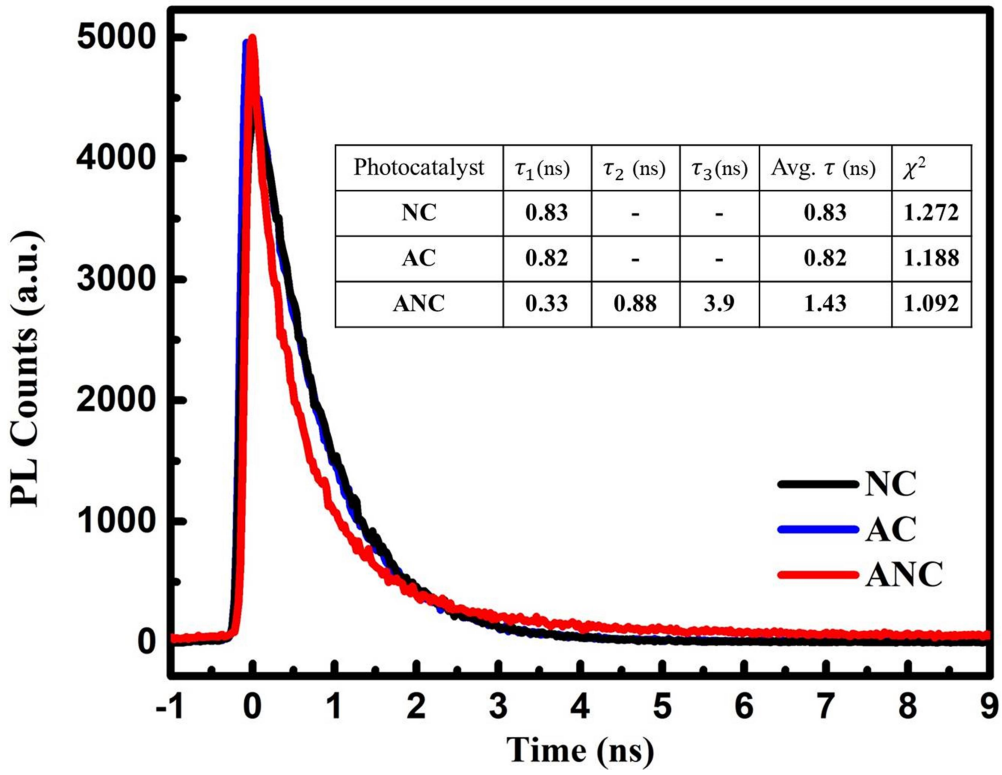

Photocatalyst	τ_1(ns)	τ_2 (ns)	τ_3(ns)	Avg. τ (ns)	χ^2
NC	0.83	-	-	0.83	1.272
AC	0.82	-	-	0.82	1.188
ANC	0.33	0.88	3.9	1.43	1.092

Figure 5.25. Time-resolved photoluminescence spectra of NC, AC, and ANC.

The extended average lifetime and delayed PL response support enhanced charge separation across the heterointerface, consistent with the establishment of a Z-scheme heterojunction in ANC. Upon initial photoexcitation of the ANC composite, comprising NiO and Ag_2CrO_4, the photogenerated charge carriers migrate efficiently across the heterointerface, thereby suppressing their rapid recombination. Furthermore, the excited electrons in the CB of Ag_2CrO_4 can undergo nonradiative relaxation to the VB of NiO, rather than radiative recombination. Following this process, band-to-band recombination of charge carriers takes place in both semiconductor components of ANC, but predominantly in Ag_2CrO_4 considering the higher electron population accumulated in its CB after electron migration from the CB of NiO. This direct recombination is therefore associated with the shortest lifetime component (τ_1) of ANC. In addition, trap-assisted interfacial recombination can occur, wherein electrons in the CB of Ag_2CrO_4 recombine with holes in the VB of NiO as a result of Z-scheme alignment of band edges. This process corresponds to the intermediate lifetime (τ_2), which is longer than τ_1. Finally, the spatially separated electrons remaining in the CB of

NiO and holes localized in the VB of Ag_2CrO_4 through the Z-scheme pathway would undergo the slowest recombination, giving rise to the longest-lifetime (τ_3). Collectively, these multicomponent decay dynamics in the TRPL spectra strongly support the proposed Z-scheme charge transfer mechanism in ANC.

5.4. Summary

In this study, Ni-Cr LDH serves as an effective precursor for the development of Ag@NiO/Ag_2CrO_4 photocatalyst through the strategic incorporation of plasmonic Ag metal. Intriguingly, thermal treatment of the LDH induces its conversion into NiO metal oxide while preserving traces of its initial hydroxide structure, $Ni(OH)_2$, thereby sustaining a complex composition poised for improved catalytic performance. The presence of metal oxide profoundly amplifies crystallinity within the structure, while Ag_2CrO_4 distinctly elevates the photocatalytic ability of the composite photocatalyst Ag@NiO/Ag_2CrO_4 (ANC). The integration of Ag offers two key benefits: it promotes the formation of Ag_2CrO_4 within the original NC matrix; and introduces Ag in its metallic state, imparting strong LSPR effects that boost electron dynamics. The heterojunction with an efficient Z-scheme charge transfer between Ag_2CrO_4 and NiO due to the intermediary role of Ag nanoparticles is one of the unique mechanisms with continuous regeneration of electron-hole pairs. Furthermore, the in-situ growth of Ag_2CrO_4 within the NC structure makes ANC a superior photocatalyst, retaining the layered architecture of the parent LDH structure while improving crystallinity and band edge alignment. The rate constant of ANC is 1.3 times higher than that of AC and 34 times higher than that of NC for the degradation of MB without sacrificial reagents. In essence, this study unveils that the intricate heterojunction matrix photocatalyst, ANC, exhibits exceptional charge carrier dynamics and synergistic effects, contributing to its highly efficient photocatalytic performance. These combined attributes make the material promising with significant prospects for future advancements in related fields. This study is in alignment with the core objectives of the thesis underlying the development of novel photocatalysts.

References

1. J. Zhang, W. Yu, J. Liu, B. Liu, Illustration of high-active Ag_2CrO_4 photocatalyst from the first-principle calculation of electronic structures and carrier effective mass, Appl. Surf. Sci. 358 (2015) 457-462.
2. M. Assis, C.C. de Foggi, V. Teodoro, J.P.D.C. da Costa, C.E. Silva, T. Robeldo, P.F. Caperuccia, C.E. Verganid, R.C. Borrac, I. Sorribese, A.F. Gouveiab, M.A. San-Miguelb, J. Andrés, E. Longo, Surface-dependent photocatalytic and biological activities of Ag_2CrO_4: Integration of experiment and simulation, Appl. Surf. Sci. 545 (2021) 148964.
3. D.G. Della Rocca, R.M. Peralta, R.A. Peralta, R.D.F. Peralta Muniz Moreira, Recent development on Ag_2MoO_4-based advanced oxidation processes: a review, React. Kinet. Mech. Catal. 132 (2021) 1-35.
4. J.C. Souza, S.C. Lemos, M. Assis, C.H. Fernandes, L.K. Ribeiro, Y. Núñez-de la Rosa, M.D. Teodoro, L. Gracia, J. Andrés, L.H. Mascaro, E. Longo, Boosted Photocatalytic Activities of Ag_2CrO_4 through Eu^{3+}-Doping Process, ACS omega., 9 (2024) 35537-35547.
5. G.S. Silva, L. Gracia, M.T. Fabbro, L.P. Serejo dos Santos, H. Beltran-Mir, E. Cordoncillo, E. Longo, J. Andres, Theoretical and experimental insight on Ag_2CrO_4 microcrystals: synthesis, characterization, and photoluminescence properties, Inorg. Chem. 55 (2016) 8961-8970.
6. A. Malathy, V. Manikandan, S. Devanesan, K. Farhat, A. Priyadharsan, C. Ragavendran, S. Ragupathy, R. Ranjith, S. Sivakumar, Development of biohybrid Ag_2CrO_4/rGO based nanocomposites with stable flotation properties as enhanced Photocatalyst for sewage treatment and antibiotic-conjugated for antibacterial evaluation, Int. J. Biol. Macromol. 244 (2023) 125303.
7. F. Yousefi, M. Haghighi, & M. Shabani, Potato-on-rod like of Z-scheme plasmon Ag_2CrO_4-$Ag_2Mo_2O_7$ heterojunction nanophotocatalyst with high stability and accelerated photo-degradation evolution of organic contaminants, Environ. Res. 236 (2023) 116853.
8. I.M. Pinatti, A.C. Tello, A.B. Trench, C.C. de Foggi, P.F. Pereira, M.M. Teixeira, N. Jacomaci, J. Andres, E. Longo, Zinc-substituted Ag_2CrO_4: a material with

enhanced photocatalytic and biological activity, J. Alloys Compd. 835 (2020) 155315.

9. Y. Du, J. Li, X. Ma, & Q. Guo, Visible light driven mesoporous ag/Ag_2CrO_4/g-C_3N_4 degrades multiple organic pollutants efficiently: Synthesis, mechanism, and degradation pathway, Vacuum. 226 (2024) 113323.
10. N. Gorouhi, M. Haghighi, M. Shabani, C.A. Jaf, Double Z-scheme Ag_2CrO_4/Bi_2O_3-KBi_6O_9Br nanophotocatalysts designed via microwave-assisted combustion-precipitation method for degrading toxic organic dyes. J. Clean. Prod. 450 (2024) 141850.
11. H. Shi, Q. Shi, X. Gu, B. Wang, B. Lumbers, G. Li, Integrating the 2D/2D heterostructure of the MXene monolayer and BiOBr nano-sheets for superior photo-catalysis, J. Colloid Interface Sci. 673 (2024) 527-536.
12. P.Y. Motlagh, A. Khataee, A. Hassani, Preparation of La-doped NiAl-LDH with boosted electron transfer for the enhanced photocatalytic activity of tetracycline: Performance evaluation, degradation pathway, and mechanism insight, J. Alloys Compd. 1008 (2024) 176448.
13. B.H. Graimed, Z.H. Jabbar, A.A. Al-Khayfawee, S.H. Ammar, H. Taofeeq, M. Al-Yasiri, The latest trends in NiAl-LDH-based heterojunctions and their photocatalytic capacity for hydrogen evolution under solar light irradiation: Photoreaction mechanism justified by DFT calculations, Int. J. Hydrog. Energy. 87 (2024) 939-965.
14. Q. Wang, D. O'Hare, Recent advances in the synthesis and application of layered double hydroxide (LDH) nanosheets, Chem. Rev. 112 (2012) 4124-4155.
15. J. Zhang, M. Gao, R. Wang, X. Li, J. Wang, S. Li, K. Cao, J. Li, Y. Wang, Z. Zheng, Bifunctional role of oxygen vacancy in LDH supported Au nanoparticles catalyst for selective photocatalytic hydrogenation of cinnamaldehyde, Fuel. 365 (2024) 131235.
16. Z.X. Bi, R.T. Guo, X. Hu, J. Wang, X. Chen, W.G. Pan, Research progress on photocatalytic reduction of CO_2 based on LDH materials, Nanoscale. 14 (2022) 3367-3386.
17. H. Boumeriame, E.S. Da Silva, A.S. Cherevan, T. Chafik, J.L. Faria, D. Eder, Layered double hydroxide (LDH)-based materials: A mini-review on strategies to

improve the performance for photocatalytic water splitting, J. Energy Chem. 64 (2022) 406-431.

18. Z.M. Mir, A. Bastos, D. Höche, M.L. Zheludkevich, Recent advances on the application of layered double hydroxides in concrete—A review, Materials. 13 (2020) 1426.
19. S.J. Xia, F.X. Liu, Z.M. Ni, W. Shi, J.L. Xue, P.P. Qian, Ti-based layered double hydroxides: efficient photocatalysts for azo dyes degradation under visible light, Appl. Catal. B: Environ. 144 (2014) 570-579.
20. W. Ye, X. Fang, X. Chen, D. Yan, A three-dimensional nickel–chromium layered double hydroxide micro/nanosheet array as an efficient and stable bifunctional electrocatalyst for overall water splitting, Nanoscale 10 (2018) 19484-19491.
21. P. Saikia, C. Gogoi, P.J. Kalita, R.L. Goswamee, Catalytic conversion of high-GWP gases N_2O and CH_4 to syngas (H_2 + CO) on SiO_2@ Ni-Cr layered nano-oxide-coated monolithic catalyst, Environ. Sci. Pollut. Res. 27 (2020) 24939-24953.
22. Y. Qu, W. Zhou, X. Miao, Y. Li, L. Jiang, K. Pan, G. Tian, Z. Ren, G. Wang, H. Fu, A New Layered Photocathode with Porous NiO Nanosheets: An Effective Candidate for p-Type Dye-Sensitized Solar Cells, Chem. Asian J. 8 (2013) 3085-3090.
23. M. Pirhashemi, A. Habibi-Yangjeh, Novel ZnO/Ag_2CrO_4 nanocomposites with n–n heterojunctions as excellent photocatalysts for degradation of different pollutants under visible light, J. Mater. Sci.: Mater. Electron. 27 (2016) 4098-4108.
24. P. Makuła, M. Pacia, W. Macyk, How to correctly determine the band gap energy of modified semiconductor photocatalysts based on UV–Vis spectra, J. Phys. Chem. Lett. 9 (2018) 6814-6817.
25. I. Chanu, P. Krishnamurthi, P.T. Manoharan, Effect of silver on plasmonic, photocatalytic, and cytotoxicity of gold in AuAgZnO nanocomposites, J. Phys. Chem. C 121 (2017) 9077-9088.
26. Z. Wang, S.K. Saxena, P. Lazor, H.S.C. O'Neill, An in situ Raman spectroscopic study of pressure induced dissociation of spinel $NiCr_2O_4$, J. Phys. Chem. Solids. 64 (2003) 425-431.

27. V. D'Ippolito, G.B. Andreozzi, D. Bersani, P.P. Lottici, Raman fingerprint of chromate, aluminate and ferrite spinels, J. Raman Spectrosc. 46 (2015) 1255-1264.
28. M. Hallassi, R. Benrabaa, N.F. Cherif, D. Lerari, R. Chebout, K. Bachari, A. Rubbens, P. Roussel, R.-N. Vannier, M. Trentesaux, A. Löfberg, Characterization and syngas production at low temperature via dry reforming of methane over Ni-M (M= Fe, Cr) catalysts tailored from LDH structure, Catalysts 12 (2022) 1507.
29. M.T. Fabbro, L. Gracia, G.S. Silva, L.P. Santos, J. Andres, E. Cordoncillo, E. Longo, Understanding the formation and growth of Ag nanoparticles on silver chromate induced by electron irradiation in electron microscope: A combined experimental and theoretical study, J. Solid State Chem. 239 (2016) 220-227.
30. O. Dvoynenko, S.L. Lo, Y.J. Chen, G.W. Chen, H.M. Tsai, Y.L. Wang, J.K. Wang, Speciation analysis of Cr (VI) and Cr (III) in water with surface-enhanced Raman spectroscopy, ACS omega. 6 (2021) 2052-2059.
31. W. Li, J. Chen, R. Guo, J. Wu, X. Zhou, J. Luo, Facile synthesis of MoS_2/Ag_2CrO_4 composites with improved visible light driven photocatalytic performance, J. Mater. Sci.: Mater. Electron. 28 (2017) 14069-14078.
32. J. Al Boukhari, A. Khalaf, R. Sayed Hassan, R. Awad, Structural, optical and magnetic properties of pure and rare earth-doped NiO nanoparticles, Appl. Phys. A. 126 (2020) 323.
33. K.V. Chandekar, M. Shkir, A. Khan, M.A. Sayed, N. Alotaibi, T. Alshahrani, H. Algarni, S. AlFaify, Significant and systematic impact of yttrium doping on physical properties of nickel oxide nanoparticles for optoelectronics applications, J. Mater. Res. Technol. 15 (2021) 2584-2600.
34. Q. Hua, T. Cao, H. Bao, Z. Jiang, W. Huang, Crystal-Plane-Controlled Surface Chemistry and Catalytic Performance of Surfactant-Free Cu_2O Nanocrystals, ChemSusChem. 6 (2013) 1966-1972.
35. Z. Zhang, H. Huo, L. Wang, S. Lou, L. Xiang, B. Xie, Q. Wang, C. Du, J. Wang, G. Yin, Stacking fault disorder induced by Mn doping in $Ni(OH)_2$ for supercapacitor electrodes, Chem. Eng. J. 412 (2021) 128617.
36. H. Chen, X. Chang, D. Chen, J. Liu, P. Liu, Y. Xue, S. Han, Graphene-karst cave flower-like Ni–Mn layered double oxides nanoarrays with energy storage electrode, Electrochim. Acta**.** 220 (2016) 36-46.

37. S. Liu, Y. Tang, C. Guo, Y. Liu, Z. Tang, Heterostructure of NiFe@NiCr-LDH for active and durable oxygen evolution reactions in alkaline media, Materials 16 (2023) 2968.
38. D. Zhu, C. Guo, J. Liu, L. Wang, Y. Du, S.Z. Qiao, Two-dimensional metal–organic frameworks with high oxidation states for efficient electrocatalytic urea oxidation, Chem. Commun. 53 (2017) 10906-10909.
39. H.Q. Wang, X.P. Fan, X.H. Zhang, Y.G. Huang, Q. Wu, Q.C. Pan, Q.Y. Li, In situ growth of NiO nanoparticles on carbon paper as a cathode for rechargeable Li–O_2 batteries, RSC Adv. 7 (2017) 23328-23333.
40. D.R. Baer, M.H. Engelhard, XPS analysis of nanostructured materials and biological surfaces, J. Electron Spectrosc. Relat. Phenom. 178 (2010) 415-432.
41. J.W. Luo, J.D. Song, W.Z. Jia, Z.Y. Pu, J.Q. Lu, M.F. Luo, Catalytic dehydrofluorination of 1, 1, 1, 3, 3-pentafluoropropane to 1, 3, 3, 3-tetrafluoropropene over fluorinated NiO/Cr_2O_3 catalysts, Appl. Surf. Sci. 433 (2018) 904-913.
42. J. Słoczyński, J. Janas, T. Machej, J. Rynkowski, J. Stoch, Catalytic activity of chromium spinels in SCR of NO with NH_3, Appl. Catal. B: Environ. 24 (2000) 45-60.
43. N. Shevchenko, V. Zaitsev, A. Walcarius, Bifunctionalized mesoporous silicas for Cr (VI) reduction and concomitant Cr (III) immobilization, Environ. Sci. Technol. 42 (2008) 6922-6928.
44. W.X. Zhang, Y. Liang, J.W. Luo, A.P. Jia, Y.J. Wang, J.Q. Lu, M.F. Luo, Morphological effects of ordered Cr_2O_3 nanorods and Cr_2O_3 nanoparticles on fluorination of 2-chloro-1, 1, 1-trifluoroethane, J. Mater. Sci. 51 (2016) 6488-6496.
45. X.Q. Li, J. Cao, W.X. Zhang, Stoichiometry of Cr (VI) immobilization using nanoscale zerovalent iron (nZVI): a study with high-resolution X-ray photoelectron spectroscopy (HR-XPS), Ind. Eng. Chem. Res. 47 (2008) 2131-2139.
46. J. Luo, X. Zhou, X. Ning, L. Zhan, L. Ma, X. Xu, Z. Huang, J. Liang, Synthesis and characterization of Z-scheme In_2S_3/Ag_2CrO_4 composites with an enhanced visible-light photocatalytic performance, New J. Chem. 41 (2017) 845-856.
47. Y. Chen, D. An, S. Sun, J. Gao, L. Qian, Reduction and removal of chromium VI in water by powdered activated carbon, Materials. 11 (2018) 269.

48. X.F. Wu, C.X. Zhang, Y.D. Wang, J.Z. Su, J.R. Zhang, Y.M. Feng, M. Zhang, X. Tong, W.-G. Zhang, X.G. Sun, Synthesis of Ag_2CrO_4/SnO_2 n–n type heterojunction as a visible light photocatalyst for degradation of rhodamine B, J. Mater. Sci.: Mater. Electron. 29 (2018) 20959-20967.
49. Y. Deng, L. Tang, G. Zeng, J. Wang, Y. Zhou, J. Wang, J. Tang, Y. Liu, B. Peng, F. Chen, Facile fabrication of a direct Z-scheme Ag_2CrO_4/g-C_3N_4 photocatalyst with enhanced visible light photocatalytic activity, J. Mol. Catal. A: Chem. 421 (2016) 209-221.
50. H. Yang, H. Hao, Y. Zhao, Y. Hu, J. Min, G. Zhang, J. Bi, S. Yan, H. Hou, An efficient construction method of S-scheme $Ag_2CrO_4/ZnFe_2O_4$ nanofibers heterojunction toward enhanced photocatalytic and antibacterial activity, Colloids Surf. A: Physicochem. Eng. Asp. 641 (2022) 128603.
51. B. Ali, E. Abdelkader, B. Naceur, C. Houcine, L. Nadjia, B. Nourredine, Sunlight-driven photocatalytic degradation of Rhodamine B by BiOCl and TiO_2 deposited on NiCr-LDH, Int. J. Environ. Anal. Chem. 103 (2023) 6722-6741.
52. K. Atacan, N. Güy, B. Boutra, M. Özacar, Enhancement of photoelectrochemical hydrogen production by using a novel ternary Ag_2CrO_4/GO/$MnFe_2O_4$ photocatalyst, Int. J. Hydrog. Energy. 45 (2020) 17453-17467.
53. X. You, F. Chen, J. Zhang, M. Anpo, A novel deposition precipitation method for preparation of Ag-loaded titanium dioxide, Catal. Lett. 102 (2005) 247-250.
54. H. Zhang, C. Liang, J. Liu, Z. Tian, G. Wang, W. Cai, Defect-mediated formation of Ag cluster-doped TiO_2 nanoparticles for efficient photodegradation of pentachlorophenol, Langmuir. 28 (2012) 3938-3944.
55. S.K. Pandey, M.K. Tripathi, V. Ramanathan, P.K. Mishra, D. Tiwary, Highly facile Ag/NiO nanocomposite synthesized by sol-gel method for mineralization of rhodamine B, J. Phys. Chem. Solid. 159 (2021) 110287.
56. M.W. Alam, A. BaQais, T.A. Mir, I. Nahvi, N. Zaidi, A. Yasin, Effect of Mo doping in NiO nanoparticles for structural modification and its efficiency for antioxidant, antibacterial applications, Sci. Rep. 13 (2023) 1328.
57. M.S. NourEldien, M.Y. Nassar, I.M. Ibrahim, H.M. Aly, Tandem NiO-Ni $(OH)_2/VS_2$ Nanosheets: A robust photocatalyst for hydrogen evolution, Mater. Adv. 5 (2024) 9107.

58. D. Xu, B. Cheng, J. Zhang, W. Wang, J. Yu, W. Ho, Photocatalytic activity of Ag_2MO_4 (M= Cr, Mo, W) photocatalysts, J. Mater. Chem. A. 3 (2015) 20153-20166.
59. A.R. Khataee, M.B. Kasiri, Photocatalytic degradation of organic dyes in the presence of nanostructured titanium dioxide: Influence of the chemical structure of dyes, J. Mol. Catal. A Chem. 328 (2010) 8-26.
60. D. Azzouni, E.M. Saoudi Hassani, Z. Rais, M. Taleb, An excellent alternative to industrial activated carbons for the purification of textile water elaborated from waste coffee grounds, Int. J. Environ. Res. 16 (2022) 89.
61. D. Dodoo-Arhin, F. P. Buabeng, J.M. Mwabora, P.N. Amaniampong, H. Agbe, E. Nyankson, D.O. Obada, N.Y. Asiedu, The effect of titanium dioxide synthesis technique and its photocatalytic degradation of organic dye pollutants, Heliyon 4 (2018) e00681.
62. Z. He, C. Sun, S. Yang, Y. Ding, H. He, Z. Wang, Photocatalytic degradation of rhodamine B by Bi_2WO_6 with electron accepting agent under microwave irradiation: mechanism and pathway, J. Hazard. Mater. 162 (2009) 1477-1486.
63. K. Yu, S. Yang, H. He, C. Sun, C. Gu, Y. Ju, Visible light-driven photocatalytic degradation of rhodamine B over $NaBiO_3$: pathways and mechanism, J. Phys. Chem. A 113 (2009) 10024-10032.
64. J. Li, M. Jiang, H. Zhou, P. Jin, K.M. Cheung, P.K. Chu, K.W. Yeung, 2019. Vanadium dioxide nanocoating induces tumor cell death through mitochondrial electron transport chain interruption. Glob. Chall. 3, 1800058.
65. H.D. Martin, C. Ruck, M. Schmidt, S. Sell, S. Beutner, B. Mayer, R. Walsh, Chemistry of carotenoid oxidation and free radical reactions, Pure Appl. Chem. 71 (1999) 2253-2262.
66. R. Basumatary, D. Konwar, B. Basumatary, A. Ramchiary, Plasmonic enhanced branched Ag sensitized Cu_2O-CuO/TiO_2 heterojunction with unprecedented photocatalytic degradation under visible light, J. Phys. Chem. Solids. 180 (2023) 111435.
67. C. Ling, C. Yue, R. Yuan, J. Qiu, F. Q. Liu, J. J. Zhu, Enhanced removal of sulfamethoxazole by a novel composite of TiO_2 nanocrystals in situ wrapped-Bi_2O_4 microrods under simulated solar irradiation, Chem. Eng. J. 384 (2020) 123278.

68. A. Alsalme, M. M. Hassan, M. A. Eltawil, A. E. Amin, A. Soltan, M. A. Messih, M. A. Ahmed, Rational sonochemical engineering of Ag_2CrO_4/g-C_3N_4 heterojunction for eradicating RhB dye under full broad spectrum, Heliyon 10 (2024) e31221.
69. S. Chen, M.N. Hossain, A. Chen, Significant enhancement of the photoelectrochemical activity of $CuWO_4$ by using a cobalt phosphate nanoscale thin film, ChemElectroChem 5 (2018) 523-530.
70. P. Li, M. Zhang, X. Li, C. Wang, R. Wang, B. Wang, H. Yan, MOF-derived NiO/CeO_2 heterojunction: a photocatalyst for degrading pollutants and hydrogen evolution, J. Mater. Sci. 55 (2020) 15930-15944.
71. Z. Shao, D. Zhang, H. Li, C. Su, X. Pu, Y. Geng, Fabrication of MIL-88A/g-C_3N_4 direct Z-scheme heterojunction with enhanced visible-light photocatalytic activity, Sep. Purif. Technol. 220 (2019) 16-24.
72. X. Pan, Y. Meng, Q. Liu, M. Xu, Construction of Ag_3PO_4/g-C_3N_4 Z-scheme heterojunction composites with visible light response for enhanced photocatalytic degradation, Molecules. 29 (2024) 3774.
73. S. Pahi, B. Mahapatra, A. Behera, S.K. Singh, R.K. Patel, Fermi level induced band edge alignment and band bending in Ag_3PO_4/Cu_2O pn heterojunction for proficient photocatalytic applications, Mater. Chem. Phys. 305 (2023) 127992.
74. A. Gangan, A. Fahmy, S.A. Shaban, Z.M. El-Bahy, Plasma modification of the structural, morphological, and catalytic activity of Fe_3O_4@SiO_2@TiO_2 core–shell system. Adv. Compos. Hybrid Mater. 8 (2025) 1-20.
75. P. Joshna, S.R. Gollu, P.M. P. Raj, B.P. Rao, P. Sahatiya, S. Kundu, Plasmonic Ag nanoparticles arbitrated enhanced photodetection in p-NiO/n-rGO heterojunction for future self-powered UV photodetectors, Nanotechnology. 30 (2019) 365201.
76. S.K. Cushing, J. Li, F. Meng, T.R. Senty, S. Suri, M. Zhi, M. Li, A.D. Bristow, N. Wu, Photocatalytic activity enhanced by plasmonic resonant energy transfer from metal to semiconductor, J. Am. Chem. Soc. 134 (2012) 15033-15041.
77. J. Li, S.K. Cushing, F. Meng, T.R. Senty, A.D. Bristow, N. Wu, Plasmon-induced resonance energy transfer for solar energy conversion. Nat. Photonics. 9 (2015) 601-607.

78. L. Zhu, K. Liu, T. Hu, W. Dong, Z. Chen, Z. Wang, UV-visible photocurrent enhancement using metal–semiconductor–metal with symmetric and asymmetric double Schottky barriers, Nanoscale 10 (2018) 12848-12854.
79. L. Kuang, Y. Zhao, W. Zhang, S. Ge, Roles of reactive oxygen species and holes in the photodegradation of cationic and anionic dyes by TiO_2 under UV irradiation, J. Environ. Eng. 142 (2016) 04015065.
80. M.A. Rauf, S.S. Ashraf, Fundamental principles and application of heterogeneous photocatalytic degradation of dyes in solution, Chem. Eng. J. 151 (2009) 10-18.
81. S. Khan, T. Noor, N. Iqbal, L. Yaqoob, Photocatalytic Dye Degradation from Textile Wastewater: A Review, ACS Omega. 9 (2024) 21751-21767.
82. A. Iborra-Torres, M. Huš, K. Nguyen, A. Vamvakeros, M.T. Sajjad, S. Dunn, M. Mertens, G. Hyett, S. Jacques, A.M. Beale, B. Likozar, S. Kellici, V. Middelkoop, 3D printed $SrNbO_2N$ photocatalyst for degradation of organic pollutants in water, Mater. Adv. 4 (2023) 3461-3472.